

A displacement-controlled arc-length solution scheme

Giuliano Pretti^{*}, William M. Coombs, Charles E. Augarde

Department of Engineering, Durham University, South Road, Durham DH1 3LE, UK

ARTICLE INFO

Article history:

Received 15 May 2021

Accepted 4 September 2021

Keywords:

Non-linear solvers
Arc-length methods
Boundary conditions
Displacement control
Large deformation mechanics
Snap-back/through

ABSTRACT

Tracing load-displacement paths in structural mechanics problems is complicated in the presence of critical points of instability where conventional load- or displacement control fails. To deal with this, arc-length methods have been developed since the 1970s, where control is taken over increments of load at these critical points, to allow full transit of the load-displacement path. However, despite their wide use and incorporation into commercial finite element software, conventional arc-length methods still struggle to cope with non-zero displacement constraints. In this paper we present a new displacement-controlled arc-length method that overcomes these shortcomings through a novel scheme of constraints on displacements and reaction forces. The new method is presented in a variety of serving suggestions, and is validated here on six very challenging problems involving truss and continuum finite elements. Despite this paper's focus on structural mechanics, the new procedure can be applied to any problems that involve nonhomogeneous Dirichlet constraints and challenging equilibrium paths.

© 2021 The Authors. Published by Elsevier Ltd. This is an open access article under the CC BY license (<http://creativecommons.org/licenses/by/4.0/>).

1. Introduction

In structural mechanics, the modelling of complex non-linear load-displacement paths poses difficulties in passing critical points, associated with instabilities found in practical engineering problems, such as buckling. These events can manifest themselves as a snap-through (non-unique displacement for a given force) or a snap-back (non-unique force for a given displacement) response in the global force-displacement behaviour of a physical problem, both of which are shown schematically in Fig. 1. Snap-through responses, shown schematically in Fig. 1a, can be captured via monotonic displacement-controlled solution advancement methods, however, monotonically increasing load-controlled simulation advancement techniques will typically fail to converge beyond point A (as shown in Fig. 2a, where there is no intersection between the top dashed line and the equilibrium path). Snap-back problems are more challenging and it is not possible to apply monotonically increasing displacement-controlled methods to problems involving snap-back, as shown in Fig. 1b, due to the non-unique nature of the displacement variation.¹ In particular, at point B of the load-displacement response in Fig. 1b, displacement-controlled schemes that monotonically increase the displacement would: (i) fail to converge or (ii) fail to capture the

complex behaviour of the structure and continue along the (or an alternative) equilibrium path missing the snap-back loop. The issues associated with using monotonically increasing displacement-controlled boundary conditions for problems involving snap-back are highlighted in Fig. 2c, where for the second vertical dashed line there are three potential solutions, shown by the red markers.

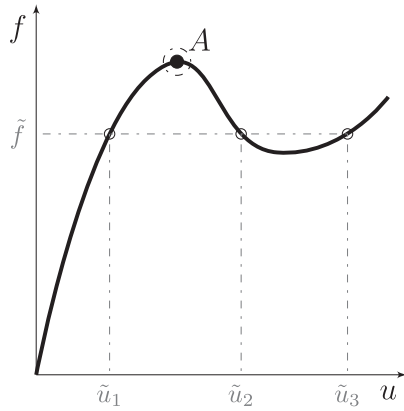
The most well-known strategy in finite element analysis to trace complex non-linear paths which include critical points is the use of arc-length methods, first introduced by Riks [33,34] and Wempner [40] in the 1970s, indeed, when implemented in commercial software these strategies are typically referred to as 'Riks' Solvers. The method allows iterative solution procedures to converge even at critical points where snap-back or snap-through behaviours occur [12,14], and is shown schematically in Fig. 2b where the arrows to the left of the figure illustrate how the force varies over the pseudo-time steps² to trace the equilibrium path. Reviews of different arc-length methods can be found in books, e.g. [14,15] and papers, e.g. [22,23], amongst others, however, to the best of the authors' knowledge, existing arc-length methods are limited to Neumann boundary conditions, that is they impose constraints on the displacement (cylindrical methods), a combination of displacement and internal force (spherical methods)

^{*} Corresponding author.

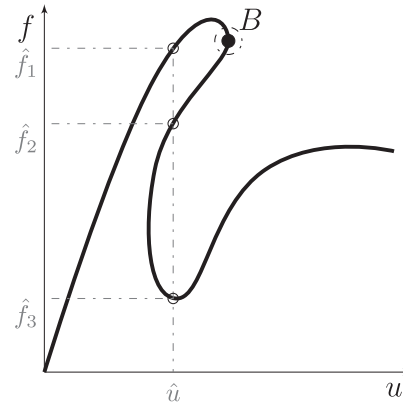
E-mail address: giuliano.pretti@durham.ac.uk (G. Pretti).

¹ Non-unique displacement variation refers to the situation where there are multiple force values for a given level of displacement.

² Pseudo-time means applying loads or displacements in incremental steps. The prefix *pseudo-* has been used as the paper focuses on quasi-static problems, where none of the considered phenomena are time-dependent. However, for the sake of brevity, in the rest of the paper we omit the *pseudo* and simply refer to these as time steps.

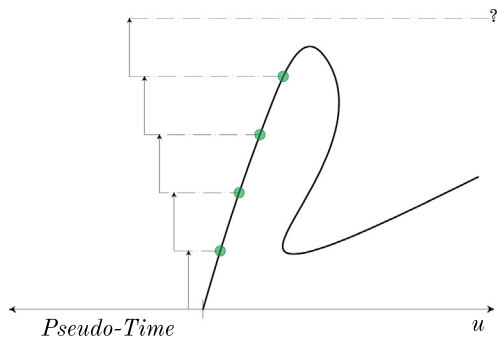


(a) Equilibrium path with snap-through (point *A*) and multiple displacements in correspondence of one force.

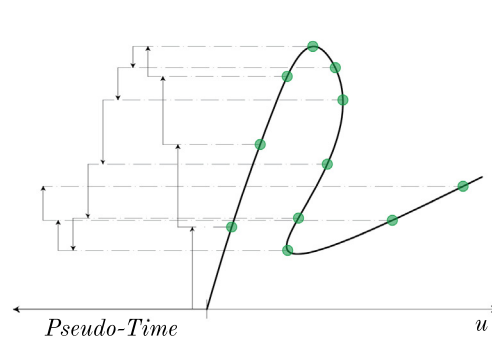


(b) Equilibrium path with snap-back (point *B*) and multiple forces in correspondence of one displacement.

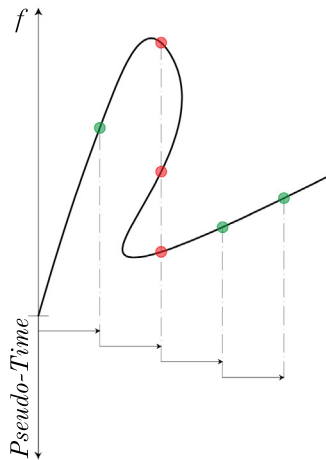
Fig. 1. Classes of unstable behaviours, where path following techniques are necessary to track the equilibrium response.



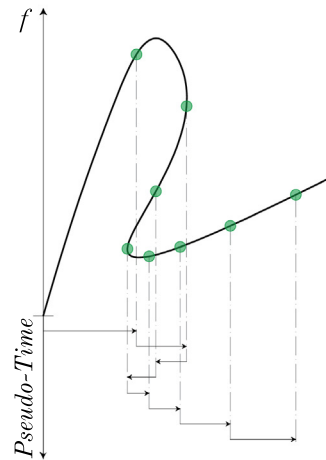
(a) Conventional monotonically increasing force-controlled analysis.



(b) Force-controlled arc-length analysis.



(c) Conventional monotonically increasing displacement-controlled analysis.



(d) Displacement-controlled arc-length analysis.

Fig. 2. Comparison of analysis methods available in the literature (a), (b) and (c), and the new method (d). The green markers indicate an intersection between the equilibrium path and the controlled parameter, whereas the red markers represent an issue in finding the equilibrium solution due to multiple intersections.

or on energy dissipated [39] by imposed nodal forces. The only boundary conditions that can be applied when adopting Riks solvers are tractions or body forces which, when integrated over the

boundary of volume of the domain, manifest themselves as equivalent nodal forces. This limits the physical problems that can be modelled using arc-length methods to those where it is

appropriate to load the analysed structure via nodal forces, however non-zero displacement constraints³ are often more appropriate especially when analysing the response of experimental tests where rigid constraints are imposed on the boundary of loaded specimens. While the initial literature on arc-length techniques is quite old, there is much evidence of their recent use in many new structural areas such as the following.

- Thin-walled structures in the post-buckling regime, e.g. Ning and Pellegrino [31], and White and Weaver [41];
- Shape morphing structures that present multiple equilibrium configurations, e.g. Diaconu et al. [17], and Arena et al. [2];
- Meta-materials whose mechanical characteristics depend on their unstable behaviour, e.g. Turco et al. [38], and Findeisen et al. [20]; and
- Brittle materials suffering damage (e.g. May et al. [30], and Gao and Bower [21]), bones [9], laminated composites [1], and graphene kirigami [3].

However, all of the above use force-controlled arc-length solution methods. Here we propose a new approach that controls prescribed displacements to follow challenging equilibrium paths that cannot be traced with existing techniques.

This paper proposes a new arc-length method that enforces constraints on the resulting nodal displacements and boundary reaction forces due to imposed nodal displacements. The method is shown schematically in Fig. 2d, where the direction and magnitude of the displacement within each time step is shown by the arrows beneath the figure. Unlike monotonically increasing displacement-controlled methods, where the direction and magnitude of the displacement is set *a priori*, in the proposed method the sign and magnitude of the imposed displacement are determined at each step based on an arc-length constraint. It is important to highlight that the proposed method controls the imposed displacement, rather than the imposed force as with existing arc-length methods, as shown in Fig. 2b. This allows physical problems to be modelled, and their associated equilibrium paths to be traced, that are not possible with existing arc-length methods that rely on the specification of nodal forces. The choice between a force- and a displacement-controlled solution scheme is driven by the boundary conditions of the physical problem being analysed. Hence, the new arc-length solution scheme should be seen as a complementary tool to solve unstable problems under displacement control, rather than as an alternative force-driven arc-length scheme. As expected when changing boundary conditions, force- and displacement-controlled equilibrium paths must generally differ. Indeed, they represent diverse solutions of the same PDE with different boundary conditions applied (Neumann in the force-driven case, Dirichlet in the displacement-driven case).

This focus here is on *strong* enforcement of Dirichlet boundary conditions. An alternative is to *weakly* enforce these boundary conditions and there are a number of different approaches in the literature, for example see [28] for a recent critique. They can be broadly split into penalty and Lagrange multiplier -type approaches. Penalty approaches require the specification of a required displacement at the controlled degrees of freedom and this is enforced by an arbitrarily specified penalty parameter which adds stiffness to the Jacobian as well as introducing an additional force component into the linear system of equations. This force could potentially be controlled using a conventional arc-length method, however care would be needed regarding the choice of

the penalty parameter to maintain coercivity and reasonable conditioning of the system of equations. Lagrange multiplier approaches and arc-length methods are perhaps a more natural combination as the Lagrange multiplier is effectively a reaction force to enforce the required displacement, and this could be controlled via an arc-length method provided that these forces are included in the equilibrium equations. However Lagrange multiplier approaches introduce an additional unknown degree of freedom for every displacement constraint, whereas our method only introduces a single additional unknown via the arc-length constraint. We therefore consider that the method described in this paper has significant advantages due to the issues associated with combining force controlled arc-length methods with penalty and Lagrange multiplier approaches discussed above and the fact that our method provides strong enforcement of the Dirichlet constraints.

This paper will focus on showing how to allow for the variation of Dirichlet boundary conditions in a finite element formulation of quasi-static equilibrium for stress analysis. The differences between the proposed displacement-controlled arc-length method and conventional load-controlled arc-length methods are highlighted by several numerical examples in Section 4 for problems involving non-linear truss and continuum elements. However, it should be appreciated that the procedures described in this paper are of wider applicability beyond structural mechanics and can be applied to any method based on a weak form, where the equations are evaluated at discrete nodal/point locations. Furthermore, it should be noted that the approach proposed here is new and does not appear in the library of schemes presented in Leon et al. [27], which unifies all of the arc-length approaches previously available in the literature. Finally, it is worth also emphasising that the current displacement-controlled arc-length method differs from the technique under the same name presented in Verhoosel et al. [39], as will be explained below.

2. Governing equations

This section outlines the governing equilibrium equations, finite element discretisation and non-linear solution method before detailing the constraint equations that can be applied to the non-linear problem to make it computationally tractable in the presence of critical points. It should be noted that most of the logic and considerations in Sections 2.1 and 2.2 differ from the classical finite element formulation, even though the final non-linear weak equilibrium equation (Eq. (8)) looks similar.

2.1. Strong and weak forms

In the case of zero body forces, let us consider the momentum balance equations applied to a body \mathcal{B} , which occupies a volume Ω in the Euclidean three-dimensional space \mathcal{E} . Let $\boldsymbol{\varphi}$ be the deformation map between the original and current configurations. On this configuration $\boldsymbol{\varphi}(\Omega)$, the Dirichlet boundary conditions are defined over the surface $\boldsymbol{\varphi}(\partial\Omega_u)$, whereas the homogeneous Neumann boundary conditions are given elsewhere on the boundary of the domain $\boldsymbol{\varphi}(\partial\Omega \setminus \partial\Omega_u)$. The above equations and conditions are classically sufficient to define the *strong form* of the problem as follows:

$$\begin{aligned} &\text{Given } \bar{\mathbf{u}} \text{ on } \boldsymbol{\varphi}(\partial\Omega_u) \text{ and the zero prescribed traction on } \boldsymbol{\varphi}(\partial\Omega \setminus \partial\Omega_u), \\ &\text{find } \mathbf{u} : \boldsymbol{\varphi}(\Omega \cup \partial\Omega) \subset \mathcal{E} \rightarrow \mathbb{R} \text{ such that} \\ &\text{div}_x \boldsymbol{\sigma} = \mathbf{0}; \quad \text{on } \boldsymbol{\varphi}(\Omega), \end{aligned} \tag{1}$$

³ It is important to highlight that zero displacement boundary condition can be included within conventional arc-length solvers as these boundary conditions do not feature in the arc-length constraint equations, which are based on non-zero nodal displacement/force values.

where $\boldsymbol{\sigma}$ is the *Cauchy stress tensor*. To clarify some of the later developments, the Dirichlet boundary conditions will be explicitly included both in the *strong form* and *weak form* of the problem. To this end, the prescribed Dirichlet boundary conditions are not only implicitly considered in the statements, but they are also unambiguously included in the forms by involving some related and unknown Neumann boundary condition values, which, in the case of stress analysis, can be physically interpreted as *reaction forces*. These forces are defined on the same boundary of the domain $\varphi(\partial\Omega_u)$, and, because of their relationship with the prescribed displacements $\bar{\mathbf{u}}$, they will be denoted as $\bar{\mathbf{t}}(\bar{\mathbf{u}})$. Moreover, as usual for prescribed Neumann conditions in stress analysis, such forces satisfy the *Cauchy theorem*

$$\bar{\mathbf{t}}(\bar{\mathbf{u}}) = \boldsymbol{\sigma}(\bar{\mathbf{u}})\mathbf{n} \quad \text{on } \varphi(\partial\Omega_u),$$

with \mathbf{n} being the outward normal vector on the considered surface. Therefore, in this method, reaction forces are not treated as they usually are in the Galerkin-based discretisation approaches (see, for instance, in the case of the finite element method, Bathe [4]). In the classical methodology, reaction forces are unknown corrections to concentrated loads that appear in the discretised (in space and time) and linearised equilibrium equations. Owing to the current methodology choice, the strong form in the above box can be stated in an alternative form as follows:

Given $\bar{\mathbf{u}}$ on $\varphi(\partial\Omega_u)$ and the zero prescribed tractions on $\varphi(\partial\Omega \setminus \partial\Omega_u)$, find $\mathbf{u} : \varphi(\Omega \cup \partial\Omega) \subset \mathcal{E} \rightarrow \mathbb{R}$ and find $\bar{\mathbf{t}}(\bar{\mathbf{u}}) : \varphi(\partial\Omega_u) \rightarrow \mathbb{R}$ such that

$$\text{div}_{\mathbf{x}} \boldsymbol{\sigma} = \mathbf{0} \quad \text{on } \varphi(\Omega); \quad (2a)$$

$$\bar{\mathbf{t}}(\bar{\mathbf{u}}) = \boldsymbol{\sigma}(\bar{\mathbf{u}})\mathbf{n} \quad \text{on } \varphi(\partial\Omega_u). \quad (2b)$$

As per practice in defining the weak form, two sets of functions are needed; these are the *trial functions*, which belong to the *kinematically admissible displacements* set \mathcal{X} of \mathcal{B} , defined by

$$\mathcal{X} = \{\mathbf{u} | \mathbf{u}(\varphi(\partial\Omega_u)) = \bar{\mathbf{u}}\},$$

and the *weighting functions*, which belong to the set

$$\mathcal{V} = \{\boldsymbol{\eta} | \boldsymbol{\eta}(\varphi(\partial\Omega_u)) = \mathbf{0}\}.$$

It can be noticed that, while the trial functions are built to satisfy the prescribed Dirichlet boundary conditions on $\varphi(\partial\Omega_u)$, the weighting functions fulfil the homogeneous conditions on the same domain. The introduction of the above-mentioned functions allows expression of the *weak form* in the following manner:

Given $\bar{\mathbf{u}}$ on $\varphi(\partial\Omega_u)$ and the zero prescribed tractions on $\varphi(\partial\Omega \setminus \partial\Omega_u)$, find $\mathbf{u} \in \mathcal{X}$ and $\bar{\mathbf{t}}(\bar{\mathbf{u}})$ such that

$$\int_{\varphi(\Omega)} \boldsymbol{\sigma} : \nabla_{\mathbf{x}} \boldsymbol{\eta} d\mathbf{v} - \int_{\varphi(\partial\Omega_u)} \bar{\mathbf{t}}(\bar{\mathbf{u}}) \cdot \boldsymbol{\eta} ds = 0, \quad \forall \boldsymbol{\eta} \in \mathcal{V}. \quad (3)$$

In continuum mechanics, this weak form is often derived from and referred to as the *Principle of Virtual Work* (see, for instance, Malvern [29]), where the physical meaning of the weighting functions $\boldsymbol{\eta}$ is related to the *virtual displacements* $\delta\mathbf{u}$, which are selected to satisfy the homogeneous Dirichlet boundary conditions on the part of the domain where these are prescribed ($\delta\bar{\mathbf{u}} = \mathbf{0}$ on $\varphi(\partial\Omega_u)$). Hence, the *virtual work* caused by reaction forces $\bar{\mathbf{t}}(\bar{\mathbf{u}})$ is zero for all the weighting functions belonging to \mathcal{V} and for all the kinematically admissible virtual displacements

$$\int_{\varphi(\partial\Omega_u)} \bar{\mathbf{t}}(\bar{\mathbf{u}}) \cdot \boldsymbol{\eta} ds = \int_{\varphi(\partial\Omega_u)} \bar{\mathbf{t}}(\bar{\mathbf{u}}) \cdot \delta\bar{\mathbf{u}} ds = 0,$$

but the reaction forces themselves are generally non-zero.

2.2. Bubnov-Galerkin approximation method

Let us introduce a canonical isoparametric finite element discretisation. Moreover, let \bar{m} denote the number of nodes on the discretised surface where prescribed displacements are given and m the remaining number of nodes such that the global number of nodes is $n_{nds}^{(g)} = \bar{m} + m$. The interpolated trial and weighting functions (denoted by the superscript h) are given by

$${}^h\mathbf{u}(\mathbf{x}) = \sum_{i=1}^m (\mathbf{u}^f)^i N_i^{(g)}(\mathbf{x}) + \sum_{j=1}^{\bar{m}} \bar{\mathbf{u}}^j N_j^{(g)}(\mathbf{x}) = \sum_{k=1}^{m+\bar{m}} \mathbf{u}^k N_k^{(g)}(\mathbf{x}); \quad (4a)$$

$${}^h\boldsymbol{\eta}(\mathbf{x}) = \sum_{i=1}^m \boldsymbol{\eta}^i N_i^{(g)}(\mathbf{x}), \quad (4b)$$

where $N^{(g)}$ are the shape functions and \mathbf{u}^f denotes the free nodal displacements, that is the displacements which are not prescribed. It can be observed that (4a) satisfies the Dirichlet boundary conditions and (4b) fulfils the homogeneous conditions on the same boundary. The number of degrees of freedom—associated with nodes where prescribed displacements are given—is $\bar{M} = n_{dim} \cdot \bar{m}$, and the remaining number is $M = n_{dim} \cdot m$. The introduction of the *global interpolation matrix* $\mathbf{N}^{(g)}$ and the *global linear strain-displacement matrix* $\mathbf{B}^{(g)}$ enables the expression of Eqs. (4) and the gradient of (4b) as follows

$${}^h\mathbf{u}(\mathbf{x}) = \mathbf{N}^{(g)}(\mathbf{x}) \mathbf{u};$$

$${}^h\boldsymbol{\eta}(\mathbf{x}) = \mathbf{N}^{(g)}(\mathbf{x}) \boldsymbol{\eta};$$

$$\nabla^h \boldsymbol{\eta}(\mathbf{x}) = \mathbf{B}^{(g)}(\mathbf{x}) \boldsymbol{\eta},$$

having introduced the notation

$$\mathbf{u} = \left[[(\mathbf{u}^f)_1^1, \dots, (\mathbf{u}^f)_{n_{dim}}^1], \dots, [(\mathbf{u}^f)_1^m, \dots, (\mathbf{u}^f)_{n_{dim}}^m], \right. \\ \left. [\bar{\mathbf{u}}_1^1, \dots, \bar{\mathbf{u}}_{n_{dim}}^1], \dots, [\bar{\mathbf{u}}_1^{\bar{m}}, \dots, \bar{\mathbf{u}}_{n_{dim}}^{\bar{m}}] \right]^T = [\mathbf{u}^f, \bar{\mathbf{u}}]^T; \quad (5a)$$

$$\boldsymbol{\eta} = \left[[\eta_1^1, \dots, \eta_{n_{dim}}^1], \dots, [\eta_1^m, \dots, \eta_{n_{dim}}^m], [\mathbf{0}], \dots, [\mathbf{0}] \right]^T. \quad (5b)$$

Therefore, the *discrete boundary value problem* formulation of Eq. (3) can be stated as

$$\left(\int_{\varphi^{(h)}(\Omega)} (\mathbf{B}^{(g)})^T \boldsymbol{\sigma} d\mathbf{v} - \int_{\varphi^{(h)}(\partial\Omega_u)} (\mathbf{N}^{(g)})^T \bar{\mathbf{t}}(\bar{\mathbf{u}}) ds \right)^T \boldsymbol{\eta} = 0 \quad \forall \boldsymbol{\eta} \in {}^h\mathcal{V}.$$

Since the above equation holds for each weighting function, it can be expressed as

$$\mathbf{f}^{int} + \mathbf{f}^{rct} = \mathbf{0}, \quad (6)$$

where the *internal force vector* and the *reaction force vector* are

$$\mathbf{f}^{int} = \int_{\varphi^{(h)}(\Omega)} (\mathbf{B}^{(g)})^T \boldsymbol{\sigma} d\mathbf{v}; \quad (7a)$$

$$\mathbf{f}^{rct} = - \int_{\varphi^{(h)}(\partial\Omega_u)} (\mathbf{N}^{(g)})^T \bar{\mathbf{t}}(\bar{\mathbf{u}}) ds. \quad (7b)$$

The above equations are assumed to be non-linear in displacement, \mathbf{u} , and therefore an incremental form of Eq. (6) is considered. Furthermore, if a backward Euler scheme is introduced to discretise the time interval, Eq. (6) becomes

$$\int_{\varphi(\Omega)} (\mathbf{B}^{(g)})^T \boldsymbol{\sigma}_{n+1} d\Omega - \int_{\varphi(\partial^h \Omega_u)} (\mathbf{N}^{(g)})^T \bar{\mathbf{t}}(\bar{\mathbf{u}}_{n+1}) = \mathbf{f}^{int}(\mathbf{u}_{n+1}) + \mathbf{f}^{rct}(\mathbf{u}_{n+1}) \approx \mathbf{0}. \quad (8)$$

Beyond this point, the subscript $n + 1$ has been omitted for convenience and to keep the equations that follow as compact as possible. (See Fig. 3)

2.3. Newton-Raphson scheme

The adoption of a backward Euler scheme leads Eq. (8) to be implicit. That is, all of the values appearing in that equation are a function of the unknown nodal displacement vector evaluated at the end of the step, \mathbf{u} . Therefore, an iterative process is necessary to solve Eq. (8) and, in the current work, a Taylor expansion is applied to adopt a Newton-Raphson scheme, which continues iterating until the out-of-balance force residual

$$\mathbf{r}(\mathbf{u}) = \mathbf{f}^{int} + \mathbf{f}^{rct} \approx \mathbf{0} \quad (9)$$

converges to a given tolerance. As stated above, the reaction force vector is defined only at the degrees of freedom belonging to the discretised domain where prescribed displacements are defined. Owing to this, we can split Eq. (9) by separating the rows related to the given displacement degrees of freedom (denoted by subscript $p = 1 \dots \bar{M}$) from those where displacements are free (indicated by subscript $f = 1 \dots M$). Accordingly, Eq. (8) can now be expressed as

$$\begin{cases} \mathbf{r}_p(\mathbf{u}) = \mathbf{f}_p^{int} + \mathbf{f}_p^{rct} \approx \mathbf{0}; & \text{(a)} \\ \mathbf{r}_f(\mathbf{u}) = \mathbf{f}_f^{int} \approx \mathbf{0}. & \text{(b)} \end{cases} \quad (10)$$

The linearisation of Eqs. (10) is performed with respect to the unknown \mathbf{u} . However, as indicated by Eq. (5a), this linearisation can be carried out by considering the prescribed displacements $\bar{\mathbf{u}}$ and the free displacements \mathbf{u}^f as two variables. Hence, the application of the Newton-Raphson scheme to Eqs. (10) leads to

$$\begin{cases} \mathbf{r}_p^{(k)}(\bar{\mathbf{u}}, \mathbf{u}^f) = \mathbf{r}_p^{(k-1)} + \left(\frac{\partial \mathbf{f}_p^{int}}{\partial \bar{\mathbf{u}}} \right)^{(k-1)} \delta \bar{\mathbf{u}} + \left(\frac{\partial \mathbf{f}_p^{int}}{\partial \mathbf{u}^f} \right)^{(k-1)} \delta \mathbf{u}^f \\ \quad + \left(\frac{\partial \mathbf{f}_p^{rct}}{\partial \bar{\mathbf{u}}} \right)^{(k-1)} \delta \bar{\mathbf{u}} + \left(\frac{\partial \mathbf{f}_p^{rct}}{\partial \mathbf{u}^f} \right)^{(k-1)} \delta \mathbf{u}^f \approx \mathbf{0}, & \text{(a)} \\ \mathbf{r}_f^{(k)}(\bar{\mathbf{u}}, \mathbf{u}^f) = \mathbf{r}_f^{(k-1)} + \left(\frac{\partial \mathbf{f}_f^{int}}{\partial \bar{\mathbf{u}}} \right)^{(k-1)} \delta \bar{\mathbf{u}} + \left(\frac{\partial \mathbf{f}_f^{int}}{\partial \mathbf{u}^f} \right)^{(k-1)} \delta \mathbf{u}^f \approx \mathbf{0}, & \text{(b)} \end{cases} \quad (11)$$

where $\delta(\bullet) = (\bullet)^{(k)} - (\bullet)^{(k-1)}$ represents the difference between the current iteration (k) and the previous iteration ($k - 1$). To further simplify Eq. (11), the tangential stiffness matrix \mathbf{K}_T can be introduced as

$$\mathbf{K}_T = \left(\frac{\partial \mathbf{f}^{int}}{\partial \mathbf{u}} \right)^{(k-1)}. \quad (12)$$

The same approach cannot be adopted to consider the linearised parts of the reaction force vector; in this case, building a matrix associated with this vector is not possible, since the reaction forces in Eq. (11) are not known. Instead the quantities related to the reaction forces will be considered as a unique linearised unknown, that is

$$\left(\frac{\partial \mathbf{f}_p^{rct}}{\partial \bar{\mathbf{u}}} \right)^{(k-1)} \delta \bar{\mathbf{u}} + \left(\frac{\partial \mathbf{f}_p^{rct}}{\partial \mathbf{u}^f} \right)^{(k-1)} \delta \mathbf{u}^f = \delta \mathbf{f}^{rct}. \quad (13)$$

Eqs. (12) and (13) allow (11) to be rewritten as

$$\begin{cases} \mathbf{r}_p^{(k)}(\bar{\mathbf{u}}, \mathbf{u}^f) = \mathbf{r}_p^{(k-1)} + \delta \mathbf{f}^{rct} + \mathbf{K}_{T,pp} \delta \bar{\mathbf{u}} + \mathbf{K}_{T,pf} \delta \mathbf{u}^f = \mathbf{0}; & \text{(a)} \\ \mathbf{r}_f^{(k)}(\bar{\mathbf{u}}, \mathbf{u}^f) = \mathbf{r}_f^{(k-1)} + \mathbf{K}_{T,fp} \delta \bar{\mathbf{u}} + \mathbf{K}_{T,ff} \delta \mathbf{u}^f = \mathbf{0}. & \text{(b)} \end{cases} \quad (14)$$

In the above equations, the subscripts of the stiffness matrix terms refer to the submatrices whose rows and columns are respectively identified by the prescribed displacements p or by those that are free f . That is, the stiffness matrix has been partitioned into the following format

$$\mathbf{K}_T = \begin{bmatrix} \mathbf{K}_{T,ff} & \mathbf{K}_{T,fp} \\ \mathbf{K}_{T,pf} & \mathbf{K}_{T,pp} \end{bmatrix}.$$

It is important to note that Eq. (14) are not directly solvable. Recalling the sizes of the unknowns

$$\dim(\bar{\mathbf{u}}) = \dim(\mathbf{f}^{rct}) = \bar{M} = n_{dim} \cdot \bar{m}; \quad (15a)$$

$$\dim(\mathbf{u}^f) = M = n_{dim} \cdot m, \quad (15b)$$

it can be observed that Eq. (14) have $2\bar{M} + M$ unknowns but only $\bar{M} + M$ equations. One way of solving this problem is to define the prescribed displacement vector as follows

$$\delta \bar{\mathbf{u}} = \delta m \bar{\mathbf{u}} \quad \text{with } \delta m \in \mathbb{R}, \quad (16)$$

where the quantity δm is a scalar unknown which expresses the magnitude and the orientation⁴ of $\delta \bar{\mathbf{u}}$. By this *modus operandi*, the number of unknowns decreases to $\bar{M} + M + 1$. The missing equation, which will be added to Eq. (14), will be provided by the so-called arc-length constraint equation, which will be discussed in Section 2.4. Besides, it is worth saying that Eq. (16) can be seen as the dual counterpart of the classical arc-length method, where the external force vector is varied via a scalar parameter (often referred to as a load factor).

2.4. Arc-length constraints

The main idea behind the constraint equation is to force the final equilibrium solution to be within a certain distance of the initial position along the equilibrium path. In this fashion, one of the principal drawbacks of the Newton-Raphson scheme, i.e. non-convergence due to the inaccuracy of the initial guess, is avoided, and solutions can be successfully found. It also allows the method to follow both snap-back and snap-through equilibrium paths.

As pointed out in SubSection 2.3, one scalar equation is necessary to complete the number of equations which, together with Eq. (14), allow the linear system of equations to be solved. As reported by Carrera [10], one of the most successful forms of constraint is that proposed by Crisfield [13] and the present work

⁴ The quantity δm expresses both the magnitude and the orientation of the vector $\delta \bar{\mathbf{u}}$ —not only the former feature—since it can be a negative value. On the other hand, $\bar{\mathbf{u}}$ describes the direction of $\delta \bar{\mathbf{u}}$.

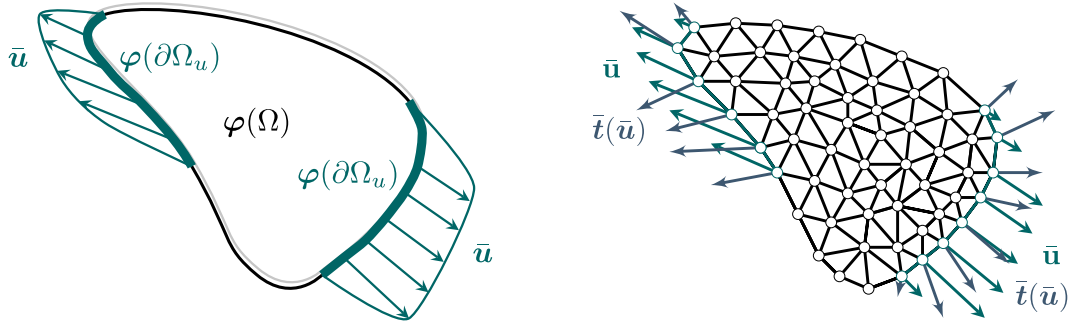


Fig. 3. Continuum problem defined by the Strong Form (1) (on the left) and discretised problem (on the right), where the reaction force vector is given by Eq. (7b).

adopts this with a minor modification. In its most general form, this constraint can be expressed as

$$g(\Delta \mathbf{u}, \Delta \mathbf{f}^{rect}, \Delta l) = g(\Delta \bar{\mathbf{u}}, \Delta \mathbf{u}^f, \Delta \mathbf{f}^{rect}, \Delta l) = 0, \quad (17)$$

where the quantities $\Delta(\bullet) = (\bullet)_{n+1} - (\bullet)_n$ are the differences between the current time interval and the previous one, and Δl is the arc-length.

2.4.1. Spherical constraint

Even though Crisfield’s modified constraint has been adopted in this work, different forms of Eq. (17) exist, depending on the quantities which are considered to contribute to the length of the arc. One particular form of constraint equation, that includes both force and displacement contributions to the arc-length, is known as a spherical constraint

$$g_{sph}(\Delta \bar{\mathbf{u}}, \Delta \mathbf{u}^f, \Delta \mathbf{f}^{rect}) = (\Delta \bar{\mathbf{u}})^T \Delta \bar{\mathbf{u}} + (\Delta \mathbf{u}^f)^T \Delta \mathbf{u}^f + \beta^2 (\Delta \mathbf{f}^{rect})^T \Delta \mathbf{f}^{rect} - \Delta l^2 = 0. \quad (18)$$

In Eq. (18), β is a scalar value used to scale the magnitude of the reaction force vector with respect to the displacements. This value can be chosen as a constant, however in problems where the global stiffness varies significantly during the analysis this may not be appropriate. Therefore, in this work the approach of Belytschko et al. [7] has been adapted to make it compatible with the proposed displacement controlled arc-length solution scheme and β is determined via

$$\beta = \left(\frac{1}{M} \sum_{i=1}^M K_{T,p_i p_i}^{(k-1)} \right)^{-1}, \quad (19)$$

where $K_{T,p_i p_i}$ is the i -th diagonal element of the submatrix $\mathbf{K}_{T,pp}$. It can be observed that Eq. (19) connects β to the trace of the tangential stiffness submatrix. In this fashion, by computing β at each iteration, we scale the external force vector with a value which is representative of the considered problem.

2.4.2. Cylindrical constraint

The cylindrical constraint can be seen as a particular case of the spherical constraint where the scalar β is set to zero, that is the arc-length is only dependent on the nodal displacements, and can be expressed as

$$g_{cyl}(\Delta \bar{\mathbf{u}}, \Delta \mathbf{u}^f) = (\Delta \bar{\mathbf{u}})^T \Delta \bar{\mathbf{u}} + (\Delta \mathbf{u}^f)^T \Delta \mathbf{u}^f - \Delta l^2 = 0. \quad (20)$$

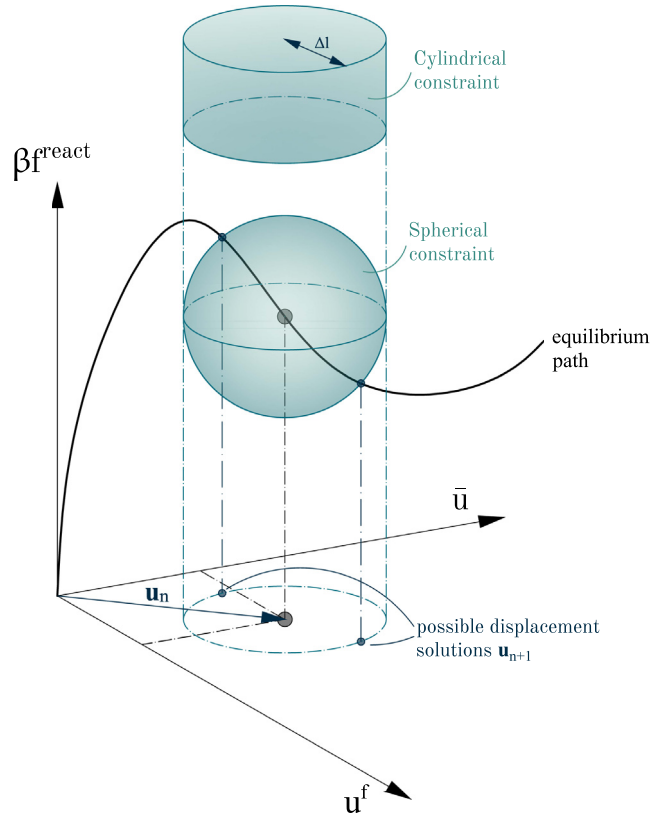


Fig. 4. Graphical representation of the cylindrical and spherical constraint for the case of $\bar{M} = M = 1$.

The graphical difference between spherical and cylindrical constraints are shown in Fig. 4, where the constraint equations are plotted in the three-dimensional axes of the prescribed displacements, the free displacements and the scaled reaction forces (in the hypothetical case of $\bar{M} = M = 1$), and it can be observed that the intersection between the equilibrium path and the constraint is more severe in the spherical case. Fig. 4 also shows that there are two intersection points between the equilibrium curve and the constraint, this point, and methods for choosing the appropriate intersection, will be discussed in Section 3.2.

3. Solution schemes

There exist several ways of applying arc-length solution schemes. In the present work, the previously established schemes for the force-controlled method have been reformulated so that they can be used with the proposed *displacement-controlled arc-length method*. A first distinction among the methods proposed in this paper is between *consistent* (Section 3.1) and *non-consistent* (Section 3.2) schemes. In addition to this, the former category of algorithms can be applied in *non-partitioned* and *partitioned* manners. The following sections explore each of the combinations.

3.1. Consistent schemes

The following schemes are labelled *consistent* (following the terminology used by Schweizerhof and Wriggers [37]) to emphasise that linearisation takes place for both equilibrium equations and constraint equation through the *Newton-Raphson* procedure. The linearised constraint form of Eq. (17) is therefore required and can be expressed as

$$\mathbf{g}^{(k)}(\Delta\bar{\mathbf{u}}, \Delta\mathbf{u}^f, \Delta\mathbf{f}^{rct}) = \mathbf{g}^{(k-1)} + \left(\frac{\partial\mathbf{g}}{\partial\bar{\mathbf{u}}}\right)^{(k-1)}\delta\bar{\mathbf{u}} + \left(\frac{\partial\mathbf{g}}{\partial\mathbf{u}^f}\right)^{(k-1)}\delta\mathbf{u}^f + \left(\frac{\partial\mathbf{g}}{\partial\mathbf{f}^{rct}}\right)^{(k-1)}\delta\mathbf{f}^{rct} \approx \mathbf{0}. \quad (21)$$

In particular, if the constraint equation is *spherical* as in Eq. (18), the linearised quantities in Eq. (21) become

$$\left(\frac{\partial\mathbf{g}_{sph}}{\partial\bar{\mathbf{u}}}\right)^{(k-1)} = 2(\Delta\bar{\mathbf{u}})^T, \quad (22a)$$

$$\left(\frac{\partial\mathbf{g}_{sph}}{\partial\mathbf{u}^f}\right)^{(k-1)} = 2(\Delta\mathbf{u}^f)^T, \quad (22b)$$

$$\left(\frac{\partial\mathbf{g}_{sph}}{\partial\mathbf{f}^{rct}}\right)^{(k-1)} = 2\beta^2(\Delta\mathbf{f}^{rct})^T. \quad (22c)$$

In the case of the *cylindrical* constraint as in Eqs. (20), (22a) and (22b) remain the same, while (22c) is equal to zero as $\beta = 0$.

3.1.1. Non-Partitioned Scheme (NPC)

In these *consistent* schemes, a *non-partitioned* solution (NPC) is applied so that the *Jacobian matrix* of the *Newton-Raphson* procedure consists of both the stiffness submatrices and the linearised quantities expressed by Eqs. (22). The resulting linear system can be expressed as

$$\begin{bmatrix} \mathbf{I} & \mathbf{K}_{T,pf} & \mathbf{K}_{T,pp}\bar{\mathbf{u}} \\ \mathbf{0} & \mathbf{K}_{T,ff} & \mathbf{K}_{T,fp}\bar{\mathbf{u}} \\ \left(\frac{\partial\mathbf{g}}{\partial\bar{\mathbf{u}}}\right)^{(k-1)} & \left(\frac{\partial\mathbf{g}}{\partial\mathbf{u}^f}\right)^{(k-1)} & \left(\frac{\partial\mathbf{g}}{\partial\mathbf{f}^{rct}}\right)^{(k-1)}\bar{\mathbf{u}} \end{bmatrix} \begin{bmatrix} \delta\mathbf{f}^{rct} \\ \delta\mathbf{u}^f \\ \delta\bar{m} \end{bmatrix} = - \begin{bmatrix} \mathbf{r}_p^{(k-1)} \\ \mathbf{r}_f^{(k-1)} \\ \mathbf{g}^{(k-1)} \end{bmatrix}, \quad (23)$$

where \mathbf{I} is the unit matrix. The sizes of the submatrices appearing in the above system are computable by the use of the dimensions given in Eq. (15).

It is important to stress that Eq. (23) is pivotal in the new method. While some papers, for instance [39,27], present techniques which look similar to a *displacement-controlled arc-length technique*, there are substantial differences between these methods and that proposed here. None of the above-mentioned approaches take into account the equilibrium equations at prescribed nodal degrees of freedom, these being Eq. (10) Therefore they fail to con-

sider the reaction forces as unknowns in Eq. (23) and do not explicitly consider equilibrium at the prescribed degrees of freedom. This omission leads in the above-mentioned papers to the need to apply a monotonic increase of prescribed displacement at the first iteration and to fix the displacement at these degrees of freedom for all the following iterations. This approach is similar to the monotonically increasing displacement-controlled analysis shown in Fig. 2c, with the difference being that the free displacements are constrained by Eq. (17) without the inclusion of the reaction forces. As a consequence, and as pointed out in [27] itself, these methods fail when trying to model snap-through. These points will be explored as part of the numerical examples in Section 4.

Predictor solution at the first interval: In order to start the analysis via Eq. (23), one arbitrary value among the three unknowns needs to be chosen *a priori*, from which the remaining unknowns can be evaluated using Eq. (23). Since the problem is solved under displacement control, it seems appropriate to set the predictor of the given displacement vector to be scaled by a positive⁵ parameter α

$$\Delta\bar{\mathbf{u}}_0^{(1)} = \alpha\bar{\mathbf{u}} \iff \alpha = \delta\bar{m}_0^{(1)} = \Delta\bar{m}_0^{(1)}. \quad (24)$$

As can be seen from the above equation, all the incremental quantities match their corresponding iterations in this particular case ($\delta\bullet = \Delta\bullet$), since no previous step has been computed for the considered problem. Owing to the setting of the initial prescribed displacements, the second line of system (23) leads the initial free displacements to be

$$\Delta\mathbf{u}_0^{f(1)} = -\alpha(\mathbf{K}_{T,ff})^{-1}\mathbf{K}_{T,fp}\bar{\mathbf{u}}.$$

Accordingly, the initial reaction force vector, which is obtained from the third line of (23), becomes

$$\Delta\mathbf{f}_0^{react(1)} = +\alpha(\mathbf{K}_{T,pf}(\mathbf{K}_{T,ff})^{-1}\mathbf{K}_{T,fp} - \mathbf{K}_{T,pp})\bar{\mathbf{u}}.$$

As suggested by Crisfield [12], the initial arc-length value can be computed by using non-linearised constraint Eq. (18), giving

$$\Delta l_0^{sph} = \alpha \left(\|\bar{\mathbf{u}}\|^2 + \|(\mathbf{K}_{T,ff})^{-1}\mathbf{K}_{T,fp}\bar{\mathbf{u}}\|^2 + \beta^2 \|(\mathbf{K}_{T,pf}(\mathbf{K}_{T,ff})^{-1}\mathbf{K}_{T,fp} - \mathbf{K}_{T,pp})\bar{\mathbf{u}}\|^2 \right)^{\frac{1}{2}}, \quad (25)$$

in the case of the cylindrical system, $\beta = 0$ and the third term vanishes. In the above, $\|\bullet\|$ is the *Euclidean norm* of \bullet . A summary of the NPC method and its application in the context of finite element analysis is given in [Algorithm 1.3.1.2. Partitioned \(PC\) Scheme](#)

As can be seen from Eq. (23), the *Jacobian matrix* is not banded, a feature that is generally useful when inverting the stiffness matrix. Therefore it can be convenient not to invert the whole *Jacobian matrix* (23) and instead solve the equations in a different way. This procedure is called the *partitioned consistent* (PC) scheme. The method is devised to solve equilibrium Eqs. (14) and the linearised constraint Eq. (21) by substitution. From Eqs. (14a) and (16) it follows that

$$\delta\mathbf{f}^{rct} = -\left(\mathbf{r}_p^{(k-1)} + \delta\bar{m}\mathbf{K}_{T,pp}\bar{\mathbf{u}} + \mathbf{K}_{T,pf}\delta\mathbf{u}^f\right), \quad (26)$$

whereas Eq. (14b) can be divided—as first suggested by Batoz and Dhett [5] for the classical arc-length method—into two parts: the first being known and the latter being a function of the scalar $\delta\bar{m}$

$$\delta\mathbf{u}^f = \delta\mathbf{u}^{NR} + \delta\bar{m}\delta\mathbf{u}^g, \quad (27)$$

where the displacement components are

⁵ The scalar value α has to be positive to ensure that the initial prescribed displacements $\Delta\bar{\mathbf{u}}_0^{(1)}$ have the same orientation of $\bar{\mathbf{u}}$.

Algorithm 1. Non-partitioned consistent (NPC) displacement-controlled arc-length pseudo-code.

```

while  $\bar{\mathbf{u}} < \text{prescribed displacements}$  do
  Set counters  $n = 0, k = 0$ ;
  Set  $\|\mathbf{r}^{(0)}\| = 2 \text{ tol}$ ;
  while  $\|\mathbf{r}^{(k)}\| > \text{tol}$  and  $k < k_{max}$  do
    Build  $\mathbf{K}_T$ ;
    Update counter  $k = k + 1$ ;
    Compute  $\beta$ , Eq. (19)  $\vee \beta = 0$ ;
    if  $k = 1$  then
      if  $n = 0$  then
        Use predictors, from Eq. (24) to (25);
      else
        Extend previous step solutions as linear predictor quantities
         $(\bullet)_{n+1}^{(1)} = (\bullet)_n + \Delta(\bullet)$ ;
      end
    else
      Solve (23);
      Update iterative variables  $\Delta \bar{\mathbf{u}}, \Delta \mathbf{u}^f, \Delta \mathbf{f}^{rect}$ ;
    end
    Compute  $\mathbf{f}^{int(k)}$ ;
    Compute  $\mathbf{r}^{(k)}$ , Eq. (6);
  end
  Set converged values as their equivalents at the end of the step  $(\bullet)_{n+1} = (\bullet)^{(k)}$ ;
  Update  $\Delta l$  (explained in Section 3.3);
  Update counter  $n + 1$ ;
end

```

$$\delta \mathbf{u}^{NR} = -(\mathbf{K}_{T,ff})^{-1} \mathbf{r}_f^{(k-1)}; \quad (28a)$$

$$\delta \mathbf{u}^g = -(\mathbf{K}_{T,ff})^{-1} (\mathbf{K}_{T,fp} \bar{\mathbf{u}}). \quad (28b)$$

Given Eqs (26,27,28a,28b), the linearised constraint Eq. (21) becomes

$$\begin{aligned} & \mathbf{g}^{(k-1)} + \delta \bar{m} \left(\frac{\partial \mathbf{g}}{\partial \bar{\mathbf{u}}} \right)^{(k-1)} \bar{\mathbf{u}} + \left(\frac{\partial \mathbf{g}}{\partial \bar{\mathbf{u}}} \right)^{(k-1)} (\delta \mathbf{u}^{NR} + \delta \bar{m} \delta \mathbf{u}^g) \\ & - \left(\frac{\partial \mathbf{g}}{\partial \mathbf{f}^{rect}} \right)^{(k-1)} \left(\mathbf{r}_p^{(k-1)} + \delta \bar{m} \mathbf{K}_{T,pp} \bar{\mathbf{u}} + \mathbf{K}_{T,pf} (\delta \mathbf{u}^{NR} + \delta \bar{m} \delta \mathbf{u}^g) \right) = 0 \end{aligned}$$

$\delta \bar{m}$ is the only unknown in the above equation and this quantity can be expressed as

$$\delta \bar{m} = - \frac{\mathbf{g}^{(k-1)} + \left(\frac{\partial \mathbf{g}}{\partial \bar{\mathbf{u}}} \right)^{(k-1)} \delta \mathbf{u}^{NR} - \left(\frac{\partial \mathbf{g}}{\partial \mathbf{f}^{rect}} \right)^{(k-1)} (\mathbf{K}_{T,pf} \delta \mathbf{u}^{NR} + \mathbf{r}_p^{(k-1)})}{\left(\frac{\partial \mathbf{g}}{\partial \bar{\mathbf{u}}} \right)^{(k-1)} \bar{\mathbf{u}} + \left(\frac{\partial \mathbf{g}}{\partial \bar{\mathbf{u}}} \right)^{(k-1)} \delta \mathbf{u}^g - \left(\frac{\partial \mathbf{g}}{\partial \mathbf{f}^{rect}} \right)^{(k-1)} (\mathbf{K}_{T,pp} \bar{\mathbf{u}} + \mathbf{K}_{T,pf} \delta \mathbf{u}^g)}. \quad (29)$$

Predictor solution at the first interval: Eq. (29) provides the direct calculation of the unknown $\delta \bar{m}$ in terms of quantities from the previous iteration within the same load (or time) step. Because of this dependency, all terms at the numerator of (29) are null when the predictor solution is evaluated at the first step. This issue can be overcome by adopting Equations from 24,25 as predictors in the PC scheme. Algorithm 2 provides the algorithm for the PC scheme. However, it is worth noting that since the algorithm for the *consistent partitioned* scheme is very close to Algorithm 1, only the grey-boxed part has been explicitly changed in Algorithm 2.

3.2. Non-Consistent (NC) Scheme

Both the methods described in Sections 3.1.1 and 3.1.2 make use of the linearised constraint Eq. (21) and, as such, they are called *consistent*. The so-called *non-consistent* scheme combines the linearised equilibrium Eq. (14) and non-linearised constraint (18).

Algorithm 2. Partitioned consistent (PC) displacement-controlled arc-length pseudo-code.

```

while  $\bar{\mathbf{u}} < \text{prescribed displacements}$  do
  ...
  while  $\|\mathbf{r}^{(k)}\| > \text{tol}$  and  $k < k_{max}$  do
    ...
    if  $k = 1$  then
      if  $n = 0$  then
        Use predictors, from Eq. (24) to (25);
      else
        Extend previous step solutions as linear predictor quantities
         $(\bullet)_{n+1}^{(1)} = (\bullet)_n + \Delta(\bullet)$ ;
      end
    else
      Compute  $\delta\mathbf{u}^{NR}$  and  $\delta\mathbf{u}^g$ , Eq. (28a) and (28b);
      Solve for  $\delta\bar{m}$ , Eq. (29);
      Compute  $\delta\mathbf{f}^{rect}$  and  $\delta\mathbf{u}^f$ , Eq. (26) and (27);
      Update iterative variables  $\Delta\bar{\mathbf{u}}$ ,  $\Delta\mathbf{u}^f$ ,  $\Delta\mathbf{f}^{rect}$ ;
    end
  end
  ...
end
  ...
end

```

In this case, only the *spherical constraint* is considered to illustrate the method. As stated above, the *cylindrical constraint* case can be obtained by setting $\beta = 0$.

To proceed, the unknown quantities $\Delta(\bullet)$ evaluated at the $k - th$ iteration are computed via their previous iteration plus their relative iterative quantity $\delta(\bullet)$, obtained from Eqs. (26) and (27), giving

$$\Delta\bar{\mathbf{u}}^{(k)} = \Delta\bar{\mathbf{u}}^{(k-1)} + \delta\bar{m} \bar{\mathbf{u}}; \quad (30a)$$

$$\Delta\mathbf{u}^f^{(k)} = \Delta\mathbf{u}^f^{(k-1)} + \delta\mathbf{u}^f = \Delta\mathbf{u}^f^{(k-1)} + \delta\mathbf{u}^{NR} + \delta\bar{m} \delta\mathbf{u}^g; \quad (30b)$$

$$\begin{aligned} \Delta\mathbf{f}^{rect(k)} &= \Delta\mathbf{f}^{rect(k-1)} + \delta\mathbf{f}^{rect} = \\ &= \Delta\mathbf{f}^{rect(k-1)} - \left(\mathbf{r}_p^{(k-1)} + \delta\bar{m} \mathbf{K}_{T,pp} \bar{\mathbf{u}} + \mathbf{K}_{T,pf} (\delta\mathbf{u}^{NR} + \delta\bar{m} \delta\mathbf{u}^g) \right) \mathbf{s}, \end{aligned} \quad (30c)$$

where the only unknown in Eq*s. (30) is $\delta\bar{m}$. The substitution of the quantities defined by (30) into the constraint Eq. (18) leads to

$$a \delta\bar{m}^2 + b \delta\bar{m} + c = 0, \quad (31)$$

where

$$a = \|\bar{\mathbf{u}}\|^2 + \|\delta\mathbf{u}^g\|^2 + \beta^2 \|\mathbf{K}_{T,pp} \bar{\mathbf{u}} + \mathbf{K}_{T,pf} \delta\mathbf{u}^g\|^2; \quad (32a)$$

$$\begin{aligned} b &= 2 \left((\Delta\bar{\mathbf{u}}^{(k-1)})^T \bar{\mathbf{u}} + (\Delta\mathbf{u}^f^{(k-1)} + \delta\mathbf{u}^{NR})^T \delta\mathbf{u}^g \right. \\ &\quad \left. + \beta^2 \left(\Delta\mathbf{f}^{rect(k-1)} - \mathbf{r}_p^{(k-1)} - \mathbf{K}_{T,pf} \delta\mathbf{u}^{NR} \right)^T (\mathbf{K}_{T,pp} \bar{\mathbf{u}} + \mathbf{K}_{T,pf} \delta\mathbf{u}^g) \right); \end{aligned} \quad (32b)$$

$$\begin{aligned} c &= \|\Delta\bar{\mathbf{u}}^{(k-1)}\|^2 + \|\Delta\mathbf{u}^f^{(k-1)} + \delta\mathbf{u}^{NR}\|^2 \\ &\quad + \beta^2 \left\| \Delta\mathbf{f}^{rect(k-1)} - \mathbf{r}_p^{(k-1)} - \mathbf{K}_{T,pf} \delta\mathbf{u}^{NR} \right\|^2 - \Delta l^2. \end{aligned} \quad (32c)$$

If a comparison of the above coefficients with those calculated for the force-controlled arc-length method (see, for instance, de Borst et al. [15]) is drawn, it can be noticed how the former resemble the latter. This should not be surprising, as Eq. (31) is obtained very similarly for both methods. Furthermore, Eq. (31) is quadratic in terms of $\delta\bar{m}$ with two roots as can also be observed in Fig. 4, since the equilibrium path intersects the constraint at two different points. In the previous *consistent* methods illustrated in Sections 3.1.2 and 3.1.1, only one root could be selected and it was performed according to the tangent direction given by the Jacobian in Eq. (23). This is one of the key differences when compared to a *non-consistent* scheme. To choose the more suitable root, a modification of the approach proposed by Crisfield [12] is adopted in this paper.⁶ In particular, the root $\delta\bar{m}$ is selected which minimises the angle between the previous iteration of the displacement vector $\Delta\mathbf{u}^{(k-1)}$ and the current one $\Delta\mathbf{u}^{(k)}$, that is

$$\begin{aligned} \delta\bar{m} &= \arg \min_{\delta\bar{m}} [(\Delta\mathbf{u}^f^{(k-1)} + \delta\mathbf{u}^{NR} + \delta\bar{m} \delta\mathbf{u}^g) \Delta\mathbf{u}^f^{(k-1)} \\ &\quad + (\Delta\bar{\mathbf{u}}^{(k-1)} + \delta\bar{m} \bar{\mathbf{u}}) \Delta\bar{\mathbf{u}}^{(k-1)}]. \end{aligned} \quad (32d)$$

However, the value of $\Delta\mathbf{u}^{(k-1)}$ is not available at the first iteration per each time step. Hence, for the *non-consistent* method, an *ad hoc* technique is necessary to overcome this issue.

⁶ The selection of the most appropriate root has received considerable attention in the arc-length literature, for example see Crisfield [14], and Ritto-Corrêa and Camotim [36] amongst others, as the correct choice of the solution direction is essential in order to trace the full equilibrium path of a problem, especially those involving snap-back/through.

Predictor solution: At the start of each load/time step (apart from the very initial load/time step which is covered below) the quadratic Eq. (31) becomes

$$a^{(1)} \delta \bar{m}^2 + c^{(1)} = 0. \quad (34)$$

The above equation has these two solutions

reader is referred to the original papers [18,19].

Predictor solution at the first interval: To start the analysis, Eq. (35) is chosen with the plus sign. In this way, $\delta \bar{m}^{(1)}$ will have

Algorithm 3. Non-consistent (NC) displacement-controlled arc-length pseudo-code.

```

while  $\bar{\mathbf{u}} < \text{prescribed displacements}$  do
  ...
  while  $\|\mathbf{r}^{(k)}\| > \text{tol}$  and  $k < k_{max}$  do
    ...
    Compute  $\delta \mathbf{u}^{NR}$  and  $\delta \mathbf{u}^g$ , Eq. (28a) and (28b);
    if  $k = 1$  then
      if  $n = 0$  then
        Compute initial arc-length  $\Delta l_0$ , Eq. (25);
        Compute  $\delta \bar{m}^{(1)}$  with positive sign, Eq. (35);
      else
        Compute  $\delta \bar{m}^{(1)}$ , Eq. (35), with sign given by Eq. (36);
      end
    else
      Compute  $a, b, c$ , Eq. (32);
      Find roots  $\delta \bar{m}$  via Eq. (31) and choose  $\delta \bar{m}$  according to Eq. (33);
      Compute  $\delta \mathbf{f}^{rct}$  and  $\delta \mathbf{u}^f$ , Eq. (26) and (27);
      Update iterative variables  $\Delta \bar{\mathbf{u}}, \Delta \mathbf{u}^f, \Delta \mathbf{f}^{rct}$ , Eq. (30);
    end
  end
  ...
end
...
Store variables  $\Delta \mathbf{u}_n^f$  and  $\Delta \bar{\mathbf{u}}_n$ ;
end

```

$$\begin{aligned} \delta \bar{m}^{(1)} &= \pm \sqrt{-\frac{c^{(1)}}{a^{(1)}}} \\ &= \pm \frac{\Delta l}{\sqrt{\|\bar{\mathbf{u}}\|^2 + \|\delta \mathbf{u}^g\|^2 + \beta^2 \|\mathbf{K}_{T,pp} \bar{\mathbf{u}} + \mathbf{K}_{T,pf} \delta \mathbf{u}^g\|^2}}. \end{aligned} \quad (35)$$

However, the appropriate root cannot be selected in the same manner as for Eq. (32d). Instead, following the idea of the *secant path* procedure proposed by Feng et al. [18,19], the sign is chosen according to the following expression

$$\text{sign}(\delta \bar{m}^{(1)}) = \text{sign}\left((\Delta \mathbf{u}_n^f)^T \delta \mathbf{u}^g + (\Delta \bar{\mathbf{u}}_n)^T \bar{\mathbf{u}}\right). \quad (36)$$

According to Riks [35], bifurcation locations are defined as points where the determinant of the tangent matrix is zero. For this reason, and as previously pointed out by [16], the secant path method does not rely on quantities which are related to the tangent matrix, being therefore insensitive to the existence of bifurcations. For further details and for an explanation of the secant path scheme, the

the same direction of the given displacement vector $\bar{\mathbf{u}}$ and the equilibrium path is not allowed to proceed in the direction opposite to the prescribed displacements for the first load/time step.

The *non-consistent* pseudo-code is presented in Algorithm 3, where, as previously described, only the grey-boxed part has been changed compared to the algorithms already presented in this paper.

3.3. Arc-lengths

To speed up the arc-length algorithms and to ensure faster convergence, the arc-lengths can vary between time intervals. The following choice comes from an extension of Crisfield's idea [12,11] and can be expressed as

$$\Delta l_{n+1} = \max \left[\min \left[\left(\frac{k^{des}}{k_n} \right) \Delta l_n, \Delta l_0 \right], \frac{\Delta l_0}{\gamma} \right], \quad (37)$$

where k^{des} is the specified desired number of Newton-Raphson iterations, k_n is the number of Newton-Raphson iterations required to converge at the previous step, and γ is a positive scalar which sets the minimum size of the arc-lengths. In this fashion, a minimum and maximum value of the arc-lengths is fixed *a priori*. Moreover, both the minimum and the maximum arc-lengths are a function of the initial values given by Eq. (25). The purpose of setting a minimum value is to balance the number of iterations and the number of time steps (see Fig. 5b). As can be seen in Fig. 5a, if this value is not used, the arc-length can keep decreasing constantly in the proximity of highly non-linear behaviour. This situation can be avoided, as graphically illustrated in Fig. 5b, by adopting Eq. (37). After reaching the peak of the projection of the equilibrium path in the $\mathbf{u}^f - \bar{\mathbf{u}}$ plane, the arc-length can start to increase again as approximately linear behaviour occurs, where the number of iterations at the previous step k_n decreases.

4. Numerical analysis

In this section, the methods described in Sections 3.1.1, 3.1.2 and 3.2 are applied to six examples to demonstrate the relative performance of the different approaches. Whenever possible, the displacement-controlled solutions have been compared to analytical results. The analysis parameters used are listed in Table 1, where a distinction is drawn between those related to the *Newton-Raphson* procedure and those necessary for the new model. In this study, geometric non-linear behaviour is considered for the finite element code cast within a *Total Lagrangian* formulation. Linear elastic constitutive models have been adopted, but, since they vary from example to example, the material parameters are specified in each of the cases below.

4.1. Single degree of freedom truss

The first validation example is the single Degree of Freedom (DoF) truss, as shown in Fig. 6, chosen because an analytical solution exists (see Bonet and Wood [8]). The problem has been solved both via the classical arc-length scheme—where the external force

vector is allowed to vary—and via the current method—where the prescribed displacement can evolve. Both of the arc-length techniques adopt the *non-consistent* procedure with a *cylindrical* constraint. The truss element consists of a *Hencky* material, with the stress and strain variables as detailed in Table 2, a Young’s modulus of $E^{(1)} = 210$ GPa and a cross sectional area of $A = 10$ cm². The initial values, which have been employed to start the simulation, are $\bar{u}_{v,0} = 3$ m and $f_{v,0} = 10$ MN, for the displacement and force controlled arc-length methods, respectively.

Fig. 7a shows that both numerical methods perfectly follow the analytical solution, without any issue in tracking the equilibrium path after the sharp snap-through at points A and B (which represent geometrically mirrored positions with respect to the horizontal direction, as shown in Fig. 7b). From points B to C, the behaviour of the structure is approximately linear, whereas geometrical non-linearity again starts to play a significant role after C. Point D represents another snap-through, even though this is much smoother than A and B. Since this example has only a single degree of freedom, the same results are expected for the force-controlled and the displacement-controlled schemes. Moreover, it should be noted that, since no snap-back takes place in Fig. 7a, the equilibrium path could be tracked by monotonically controlling the displacements. The novelty of the new method will be emphasised by the next example, where a distinction between the force-controlled and the displacement-controlled analysis will be highlighted.

However, before moving to the next example, a brief study varying the parameter α is presented for the displacement-controlled method using the NC scheme with the cylindrical constraint. The results are summarised in Table 3, with all the equilibrium paths tracing that represented in Fig. 7a and the analyses being stopped after the vertical displacements had exceeded 4 m. It is noticeable that the maximum number of iterations $\max k_{n+1}$, when equal to or higher than 6, leads to a continuous change in the number of different arc-lengths used ($N_{\alpha} \neq l_{n+1}$), 10 for $\alpha = 0.1$ and 6 for $\alpha = 0.05$ respectively. These constant oscillations comply with the choice of $k^{des} = 5$. The lowest number of iterations $\min k_{n+1}$ is 4 for most simulations, with the exception of $\alpha = 0.001$,

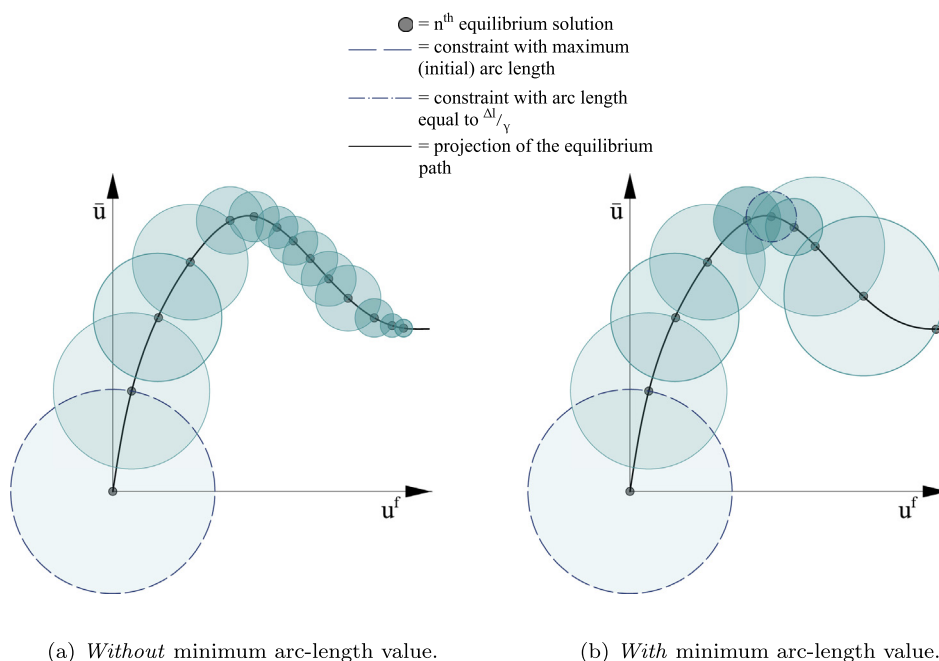


Fig. 5. Variations of arc-lengths with $\bar{m} = m = 1$.

Table 1
Convergence criteria and displacement-controlled arc-length scheme parameters.

Parameter Settings		
Convergence Parameters	tol	1×10^{-9}
	k^{des}	5
	k^{max}	20
Model Parameters	α	10^{-2}
	γ	4

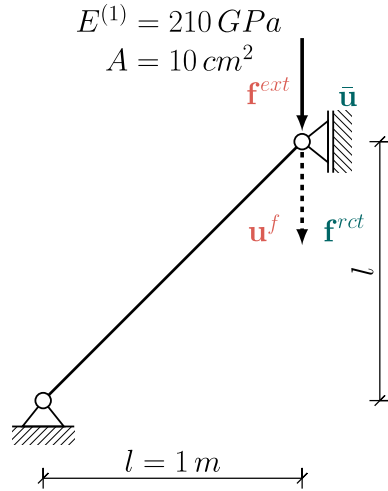


Fig. 6. Single DoF truss geometry and features in case of load control and in case of displacement control.

where this value is 3. Nonetheless, in this last case, it can be seen from the mean value of iterations per step $\bar{k}_{n+1} \approx 3.96$ that the minimum value of 3 iterations happens once in the whole simulation. A qualitative relationship appears to exist between the order of magnitude of α , the mean value of iterations \bar{k}_{n+1} , the total number of iterations $\sum_{n+1}^T k_{n+1}$, and the number of time steps T . $\alpha = 0.1$ and $\alpha = 0.05$ give a mean value of iterations close to 5, between 84 and 93 total iterations, and from 16 to 18 time-steps. The mean value of iterations decreases for $\alpha = 0.01$ ($\bar{k}_{n+1} \approx 4.85$) and for $\alpha = 0.005$ ($\bar{k}_{n+1} \approx 4.15$). Moreover, for these values of α , there is an expected net growth in the number of total iterations ($\sum_{n+1}^T k_{n+1} = 165,199$) and in the number of time steps ($T = 34,48$) respectively. The same trends can be seen for $\alpha = 0.001$, with a further increase in the total value of iterations ($\sum_{n+1}^T k_{n+1} = 420$) and the number of time-steps ($T = 106$). Overall, $\alpha = 0.01$ appears to be a good compromise between performance and stability. Nonetheless, the authors acknowledge that this value is highly problem-dependent and should be tailored to the circumstances.

4.2. Two-member truss

The two-member truss in Fig. 8a has been previously studied by Pecknold et al. [32] and by Yang and Shieh [42], where the analyses

Table 2
Different material assumptions, with respective stress-strain relationships, used in the numerical examples.

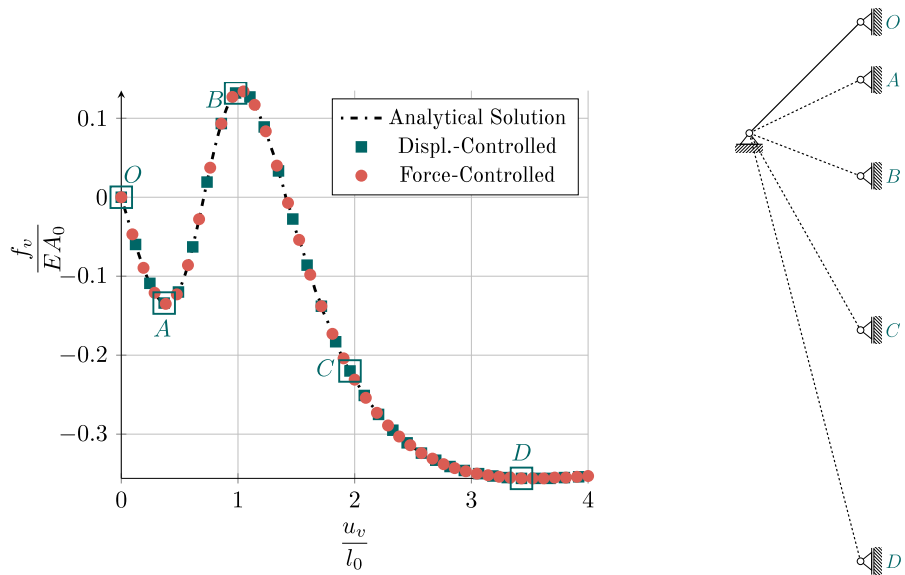
Material Name	Stress Tensor	Strain Tensor	Young's Modulus
Hencky	Kirchhoff	Logarithmic	$E^{(1)}$
Saint Venant-Kirchhoff	Second Piola-Kirchhoff	Green-Lagrange	$E^{(2)}$

were run under force control. To permit direct comparison, imperial units have been adopted here. As can be observed from Figs. 8b and c, two degrees of freedom are allowed to vary in these analyses, with the horizontal values of displacement or force being a fixed ratio of the respective vertical ones. Since the structural behaviours are dependent on more than a single degree of freedom, the equilibrium paths will be significantly different when considering either force-controlled or displacement-controlled analyses (see Figs. 9 and 11, and corresponding deflection shapes in Figs. 10 and 12)). In the latter cases, the results have been compared to their respective analytical solutions (reported in Appendix A), which, to the authors' knowledge, are not available in the literature. Even in this case, it should be stressed that a rigorous assessment of the new methodology is provided by the analytical formula, leading to the perfect overlap of the equilibrium paths shown in Figs. 9 and 11.

The initial values for starting the analyses are $\bar{u}_{v,0} = 39.37$ in and $f_{v,0} = 180$ lb In this case, the cylindrical constraint has been used along with the non-consistent scheme. Two constitutive relationships, i.e. Hencky and Saint Venant-Kirchhoff materials (see Table 2) are used and the structural behaviours are shown in Figs. 9 and 11, Young's moduli $E^{(1)}$ and $E^{(2)}$ having the same numerical value (see Fig. 8a). The choice of different stress-strain relationships has been made both to underline the differences in force-controlled and displacement-controlled analyses, and to prove the effectiveness of such techniques in different tests.

Considering the Hencky material, the equilibrium path traced by the force-controlled analysis contains several snaps-through and snaps-back (Fig. 9b and d), whereas the path resulting from a displacement-controlled method has only snap-through points. Fig. 9a shows that the structural behaviours expressed in the $u_v - f_v$ plane are practically similar, with slightly higher peaks (points A and C) in the displacement-controlled analysis. As can be noted from all of the plots in Fig. 9 for the force-controlled approach, there exists a configuration (slightly before point B') with null internal forces and zero horizontal displacement. This configuration originates when the vertical displacement is precisely the same as the height of the structure $u_v = l = 25.85$ in, leading the top pin to be at the same level of the supports. If a small step forward of the same vertical displacement is considered for the displacement-controlled analysis, a peak of horizontal reaction force is obtained (shortly after point B in Figs. 9c and d).

In the Saint Venant-Kirchhoff model, the equilibrium paths traced in Fig. 11 present several snap-throughs for both analyses, whereas there are some snap-backs only when the test is run under force control. In the latter case, the equilibrium path happens to be remarkably convoluted if compared to the monotonically increasing one resulting from a displacement-controlled test. Unlike the Hencky material, the Saint Venant-Kirchhoff model leads to different magnitudes of the vertical force peaks (A for displacement-controlled and A' for force-controlled analysis, see Fig. 11a). Nonetheless, the equilibrium paths illustrated in Fig. 11a show that there are some overlays between the points A and C for the displacement-controlled analysis and the points D' and C' for the force-controlled case in the $u_v - f_v$ plane. Overall, when the displacement-controlled method is applied, the structural response includes two mirrored peaks A and C, and a zero vertical



(a) Load-displacement curves. $l_0 = l\sqrt{2}$ is the original length of the truss.

(b) Deformation stages.

Fig. 7. Single DoF truss behaviour.

Table 3
Comparative study on the role of α .

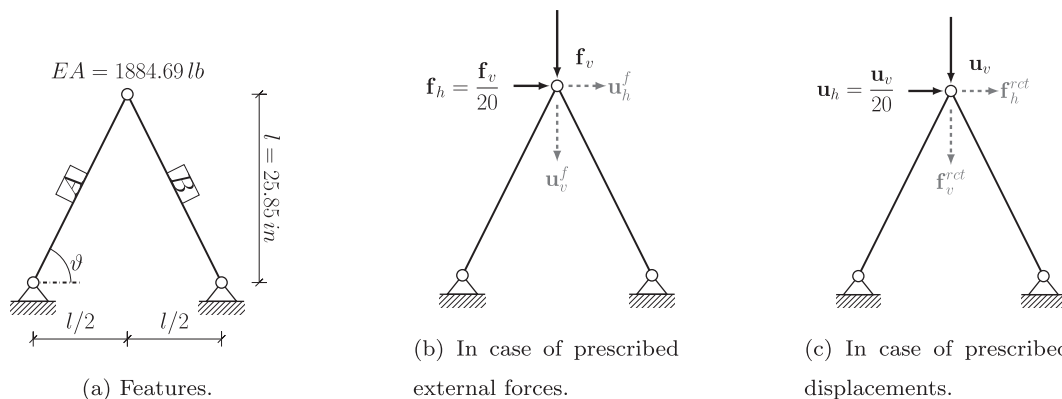
	$\max k_{n+1}$	$\min k_{n+1}$	\bar{k}_{n+1}	$\sum_{n+1}^T k_{n+1}$	T	No $\neq l_{n+1}$
$\alpha = 0.1$	6	4	5.25	84	16	10
$\alpha = 0.05$	6	4	≈ 5.17	93	18	6
$\alpha = 0.01$	5	4	≈ 4.85	165	34	1
$\alpha = 0.005$	5	4	≈ 4.15	199	48	1
$\alpha = 0.001$	4	3	≈ 3.96	420	106	1

force point B. However, unlike the Hencky material, this constitutive relationship does not lead to a peak in the horizontal reaction forces in correspondence of B (Figs. 11c and d).

To provide a detailed overview of the different techniques explained in Section 3, a parametric study varying the stress-strain relationships (Hencky and Saint Venant - Kirchhoff materials) was run. The set-up values are in Table 1, and the analyses were stopped after the vertical displacements had exceeded 55". The results, which perfectly follow the equilibrium paths illustrated in Figs. 9 and 11, are summarised in Table 4.

The general trend, indicated by the lowest values of time steps $T = 88$ and by the total number of iterations $\sum_{n+1}^T k_{n+1} = 264$, shows that the NC scheme with the cylindrical constraint is the best performing option for both materials. In addition, the percentages of time steps with minimum and maximum arc sizes are the same, i.e. $\% @ l_{min} = \% @ l_{max} = 100\%$. This uniformity, as well as the constant average of iterations per step ($\bar{k}_{n+1} = 3$), appears to confirm the algorithm's stability and the NC scheme with the cylindrical constraint can be regarded as the most reliable when dealing with convoluted equilibrium paths. However, when the NC scheme is applied with the spherical constraint, the behaviour changes dramatically. The persistent shrinkage of the arc length, highlighted by the convergence becoming linear ($\bar{k}_{n+1} \rightarrow 1$), makes the number of time steps necessary to achieve the target solution $u_v = 55''$ grow to infinity ($T \rightarrow \infty$).

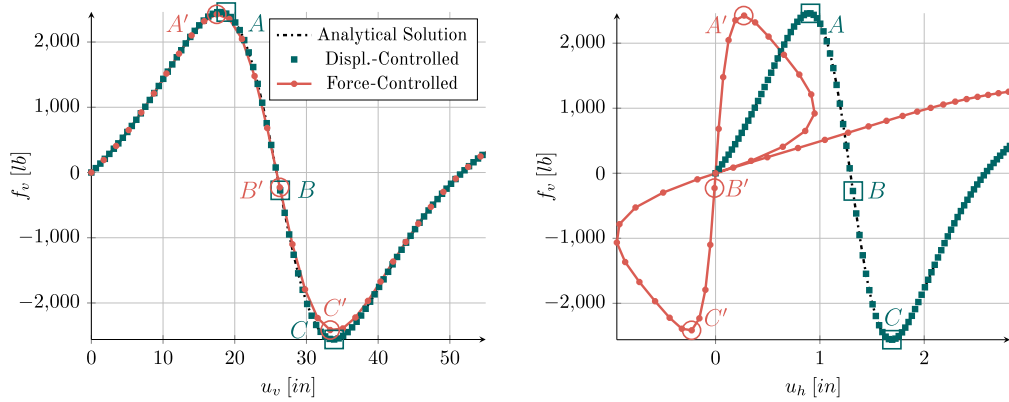
On the other hand, the NPC scheme is the only case where the spherical constraint performs better than the cylindrical. This benefit is due to the spherical constraint's positive impact on the condition number of the Jacobian. This improvement does not occur in



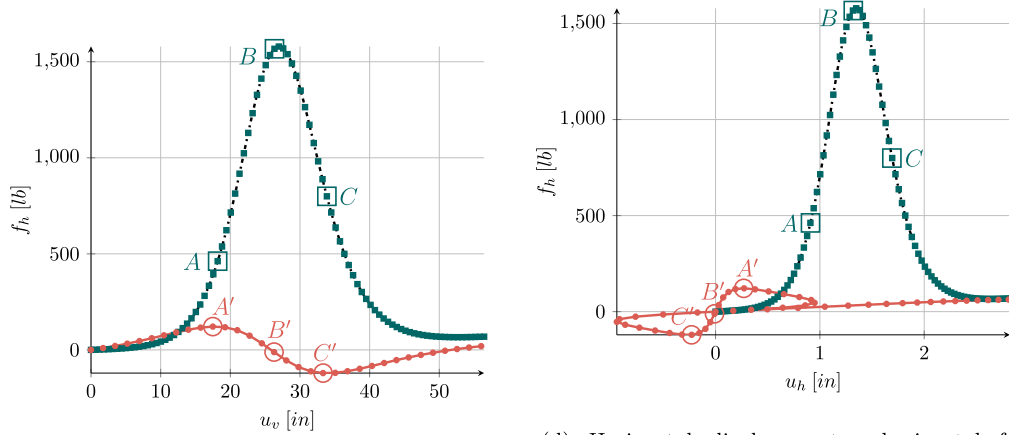
(b) In case of prescribed external forces.

(c) In case of prescribed displacements.

Fig. 8. Two-member truss.



(a) Vertical displacement - vertical force curve. (b) Horizontal displacement - vertical force curve.



(c) Vertical displacement - horizontal force curve. (d) Horizontal displacement - horizontal force curve.

Fig. 9. Two-member truss load-displacement curves for a Hencky material.

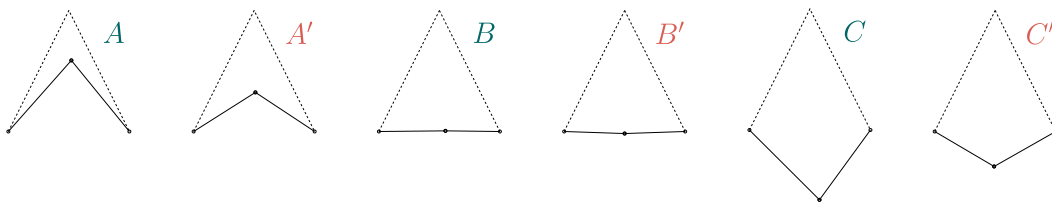


Fig. 10. Deflection shapes of the Hencky model two-member truss arch under displacement control and under force control.

the cylindrical case, with the inversion of the Jacobian failing at the first step for both materials.

From Table 4, it is appreciable how, in the PC scheme, the use of both constraints leads to successful completion for either material. However, as most of the considered parameters indicate, i.e. maximum number of iterations in one step $\max k_{n+1}$, average iterations per time steps \bar{k}_{n+1} , the total number of iterations $\sum_{n+1}^T k_{n+1}$, and the number of time steps T , the spherical constraint performs worse than its cylindrical counterpart, with higher values in all the above.

4.3. 3D dome

In this example, the star dome shown in Fig. 13 is considered. The same example appears in Geers [22], Kamat et al. [25], Kwok et al. [26] and Bellini and Chulya [6], all of which used force-

controlled schemes. Here, in contrast, we analyse the same geometry using the proposed displacement-controlled scheme. This structure has twelve supports distributed along a perimeter with a radius of 60 m, with a pin every 30°. Six other pins, positioned on an internal circle with a radius of 30 m, are situated at a height of 4.5 m. The top pin is placed at a height of 6 m and the vertical displacement, \bar{u} , is applied at this point. All of the members have the same cross sectional area, $A = 10 \text{ cm}^2$, and adopt a Hencky material model with $E^{(1)} = 210 \text{ GPa}$.

This example has been chosen for two practical reasons: (i) results are presented at a single degree of freedom and, as such can be compared between force-controlled and displacement-controlled analyses and (ii) the complicated structural response—presents several snaps-through and snaps-back, which the classical monotonically increasing displacement-controlled analysis cannot handle. Hence, all of the methods described have been applied and

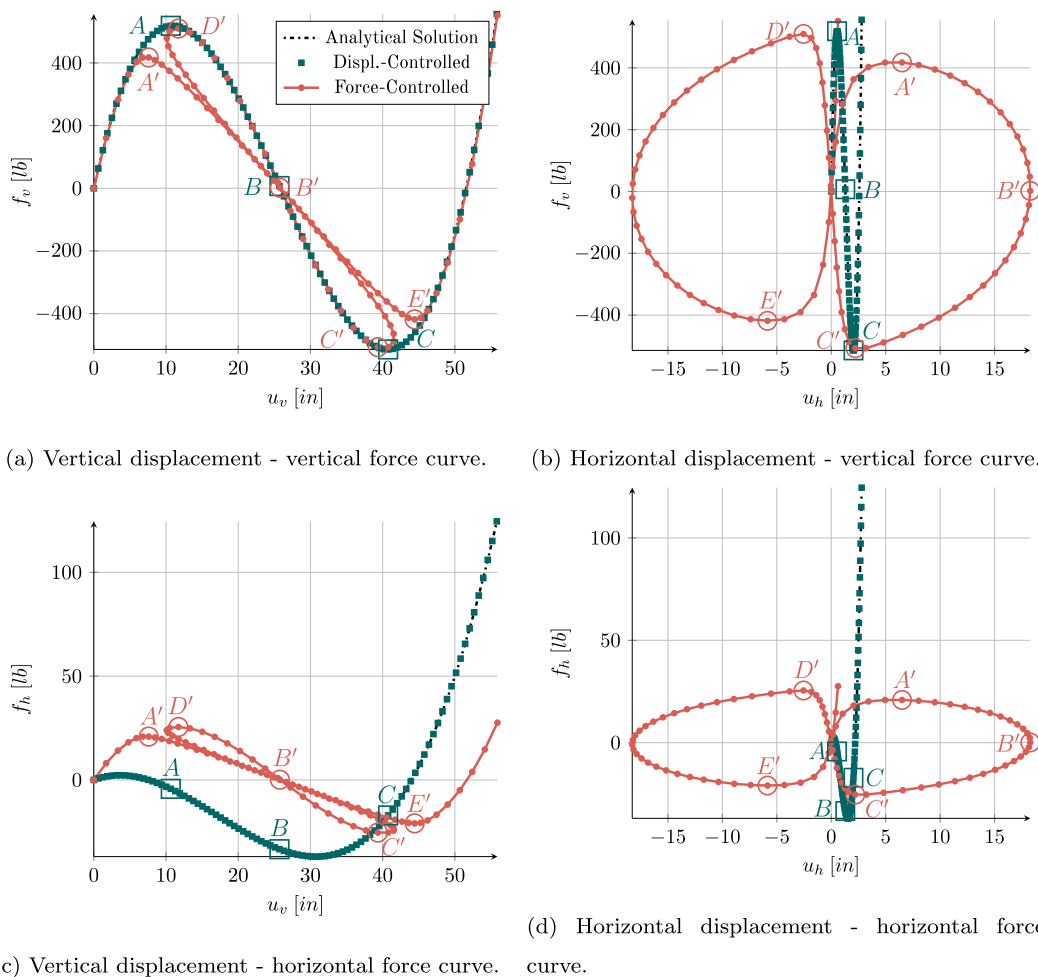


Fig. 11. Two-member truss load-displacement curves for a Saint Venant-Kirchhoff material.

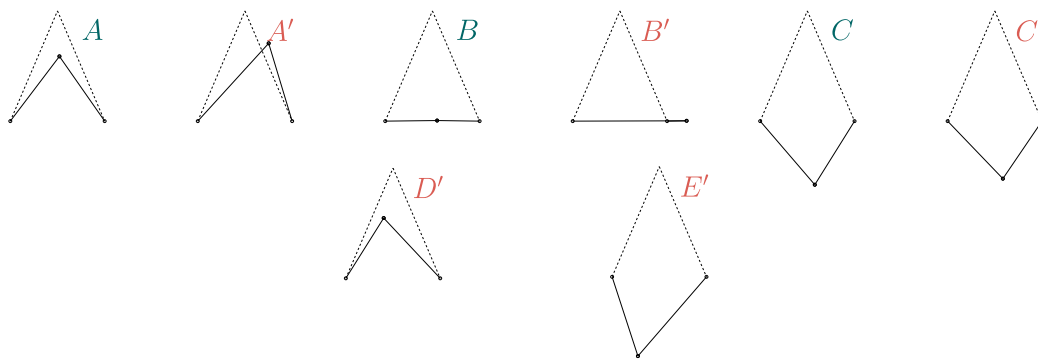


Fig. 12. Deflection shapes of the Saint Venant-Kirchhoff model two-member truss arch under displacement control and under force control.

cylindrical and spherical constraints considered in each case. The parameters necessary to run the analyses are presented in Table 1, with the exception of α which is set as 1. This change in the α parameter is due to the geometry of the dome modelled. All of the tests start with the vertical displacement value Δu_0 of 3 m and have been stopped when the vertical displacement exceeds 15 m.

As can be observed from Fig. 14, the structure has a highly non-linear response. At first, between O and A, an initial stiffening is immediately followed by a softening ending at A. It should be

noted that the vertical displacement value of A is 3 m, meaning that the top pin is mirrored along the horizontal plane defined by a height of 4.5 m. From A to B, the dome regains stiffness due to the involvement of the trusses in the outer circle. However, this part of the structural behaviour is non-linear too, with the curvature of the load-displacement curve changing. After B, there is a drop in the force response since the outer layer of elements buckle (see the deflected shape C in Fig. 14). From point C to D, the top pin is pulled up again, with the outer layer of elements being almost horizontal. D is followed by another sharp fall (and

Table 4
Performance results for different displacement-controlled arc-length solution schemes.

Material	Considered Scheme		max k_{n+1}	min k_{n+1}	\bar{k}_{n+1}	$\sum_{n+1}^T k_{n+1}$	T	% @ l_{min}	% @ l_{max}
Hencky	NPC	Sph.	8	3	≈ 3.60	1115	310	$\frac{3}{310} \approx 0.97\%$	$\frac{305}{310} \approx 98.4\%$
		Cyl.	-	-	-	-	†1	-	-
	PC	Sph.	10	3	3.6	1116	310	$\frac{2}{310} \approx 0.65\%$	$\frac{305}{310} \approx 98.39\%$
		Cyl.	6	2	≈ 2.04	286	140	$\frac{1}{140} \approx 0.71\%$	$\frac{139}{140} \approx 99.29\%$
	NC	Sph.	4	1	$\rightarrow 1$	$\rightarrow \infty$	† ∞	-	-
		Cyl.	3	3	3	264	88	$\frac{88}{88} = 100\%$	$\frac{88}{88} = 100\%$
Saint Venant - Kirchhoff	NPC	Sph.	8	1	≈ 3.11	2260	727	$\frac{44}{727} \approx 6.05\%$	$\frac{525}{727} \approx 72.08\%$
		Cyl.	-	-	-	-	†1	-	-
	PC	Sph.	10	1	≈ 3.13	2296	734	$\frac{45}{734} \approx 6.13\%$	$\frac{521}{734} \approx 70.98\%$
		Cyl.	6	2	≈ 2.04	286	140	$\frac{1}{140} \approx 0.71\%$	$\frac{139}{140} \approx 99.29\%$
	NC	Sph.	4	1	$\rightarrow 1$	$\rightarrow \infty$	† ∞	-	-
		Cyl.	3	3	3	264	88	$\frac{88}{88} = 100\%$	$\frac{88}{88} = 100\%$

† Arc length kept shrinking.
‡ Analysis failed.

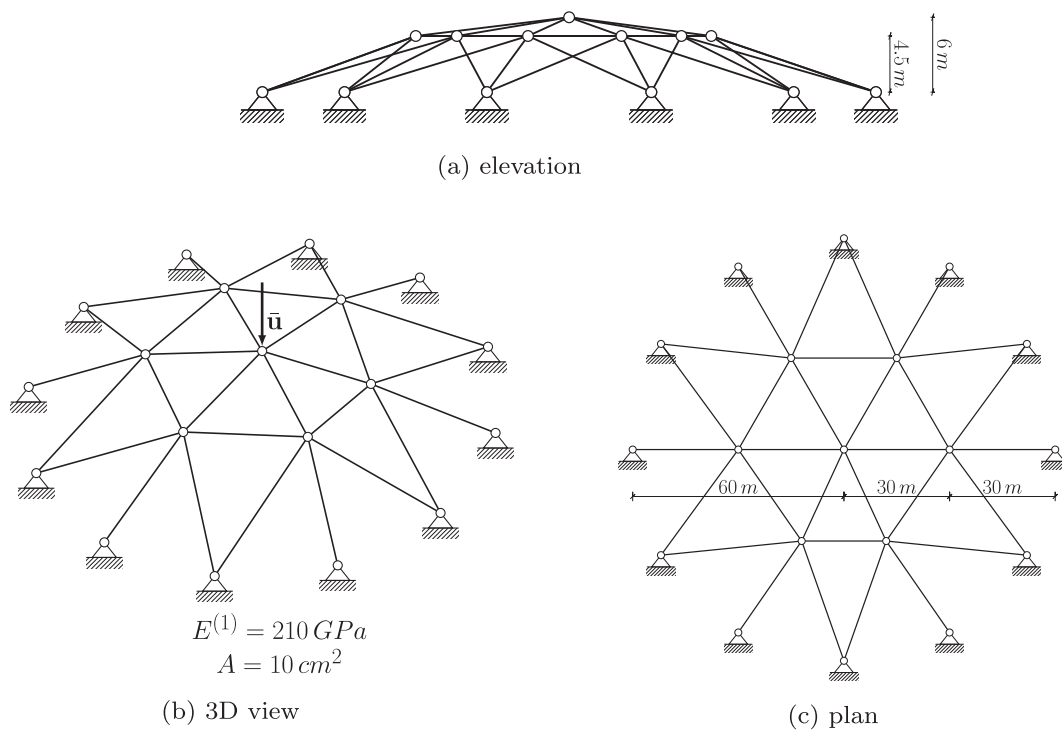


Fig. 13. Dome geometry and boundary conditions.

change in sign) in the force response, which culminates in E , the lowest point of the structural behaviour. Then, from E to F , the dome responds similarly to the part from A to B . After the point F , its stiffness due to its geometrical configuration is very low and beyond this point, as confirmed by the configuration G in Fig. 14, the geometry of the dome has been completely reversed compared to the original configuration shown in Fig. 13.

In Table 5, some values necessary for evaluating the convergence of the different displacement-controlled schemes have been collected. Some of these results relate to the *Newton-Raphson* method, i.e. the maximum and minimum number of iterations k_i occurring within a time step, and the total number of iterations which have been necessary to complete the analyses. Some other data depend on the overall behaviour during the tests, for instance, the total number of time steps T to achieve a vertical dis-

placement exceeding 15 m, and the percentages resulting from the ratio between the number of time-steps where the minimum (or the maximum) size of the arc-length has been employed by the algorithm and the total time-steps, T . These values are enumerated under the headings % @ l_{min} and % @ l_{max} . Moreover, the definition of the *utilisation index* is introduced as

$$e_u = \frac{1}{T} \sum_{n+1}^T \frac{\Delta l_{n+1} - \Delta l_{min}}{\Delta l_{max} - \Delta l_{min}}, \quad \text{with } e_u \in [0, 1].$$

This value is an indirect measure of algorithm performance: the closer it is to zero, the more the algorithm struggles to achieve convergence, whereas a value of 1 means that the maximum arc-length size is used in all of the iterations.

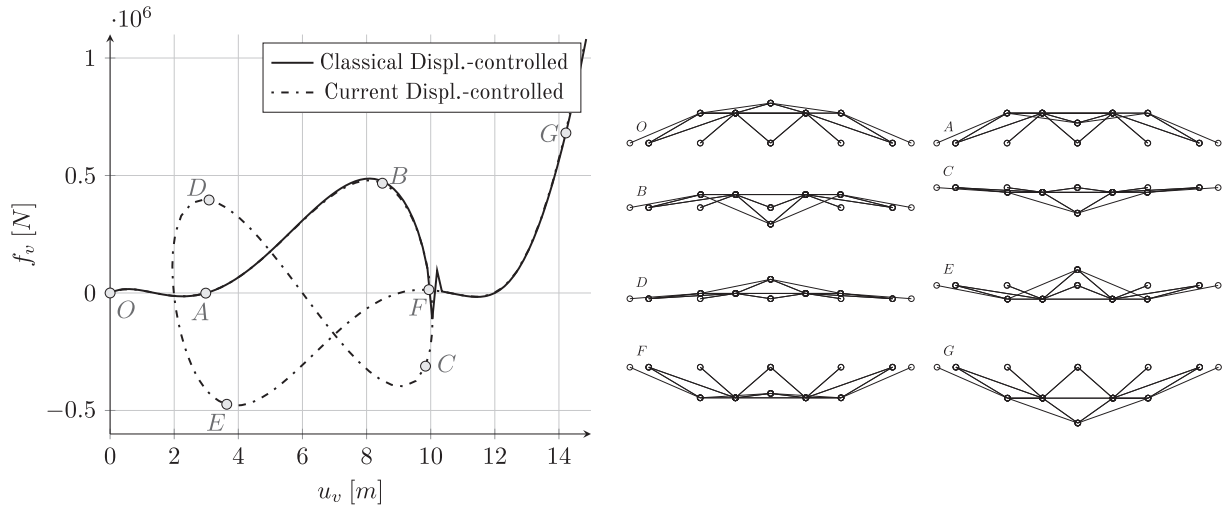
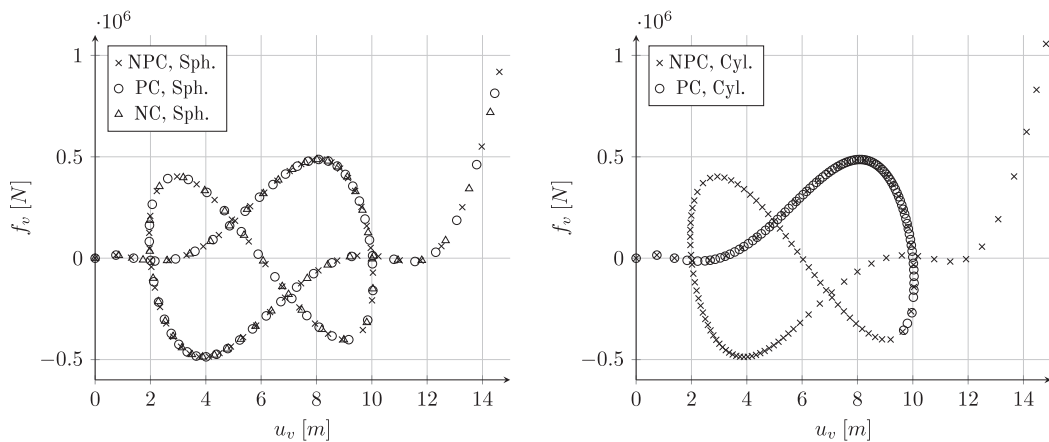


Fig. 14. Dome structural response: load-displacement curve traced by force-controlled method (on the left) and some of the relative deflection shapes (on the right).

Table 5 Performance results for different displacement-controlled arc-length solution schemes.

Considered Scheme		$\max k_{n+1}$	$\min k_{n+1}$	$\sum_{n+1}^T k_{n+1}$	T	% @ l_{min}	% @ l_{max}	ϵ_u
NPC	Sph.	7	4	296	67	$\frac{2}{67} \approx 2.99\%$	$\frac{53}{67} \approx 79.1\%$	89.7%
	Cyl.	7	4	606	120	$\frac{5}{120} \approx 4.17\%$	$\frac{27}{120} = 22.5\%$	47.4%
PC	Sph.	7	4	291	66	$\frac{1}{66} \approx 1.52\%$	$\frac{57}{66} \approx 86.4\%$	92.2%
	Cyl.	20	6	947	†87	$\frac{63}{87} \approx 72.4\%$	$\frac{1}{87} \approx 1.15\%$	2.52%
NC	Sph.	5	4	266	57	$\frac{0}{57} = 0\%$	$\frac{57}{57} = 100\%$	100%
	Cyl.	-	-	-	†1	-	-	-

† Analysis failed.



(a) Load-displacement curve for spherical constraint.

(b) Load-displacement curve for cylindrical constraint.

Fig. 15. Dome structural response for all of the displacement-controlled arc-length solution schemes.

Considering the performance of the *spherical* constraint (where the force-displacement response is shown in Fig. 15a), it can be seen that all of the algorithms converge, with the NC scheme being marginally more efficient. It can be observed that this scheme does not exceed the number of the desired iterations, meaning that the arc-length size does not change in the simulation, leading to the over-

all number of time-steps to equalling that where the maximum arc-length size has been employed. The *non-partitioned consistent* (NPC) and the *partitioned consistent* (PC) methods behave similarly, with *utilisation* values of 89.7% and 92.2% (see Table 5); this may be predictable since the same mathematics underlies these two methods, although the equations are solved differently.

If the *cylindrical* constraint is considered instead (where the force-displacement response can be seen in Fig. 15b), the *non-partitioned consistent* scheme is the only scheme that can trace the whole structural response, even though it takes almost twice as many time steps as its respective *spherical* constraint. This trend is confirmed by the value of the *utilisation index* of 47.4%, whereas this increases to 89.7% for the *spherical* constraint case. Both the PC and the NC schemes fail if the *cylindrical* constraint is applied, but for different reasons: the former starts to struggle to converge and backtracks along the equilibrium path, whereas the latter does not even start. As the interruption in the PC analysis is a consequence of algorithm failure, it is possible for the NC method to reproduce some of the equilibrium path if different values of α or different initial vertical displacement are imposed. However, it is then necessary to reduce the initial arc-length size defined by Eq. (25) to reproduce the entire equilibrium path using the NC approach.

4.4. Crisfield arch

The bi-dimensional arch in Fig. 16 was first analysed by Crisfield [14], and appears in other papers, e.g.[24]. However, to demonstrate the difference between a force-controlled and a displacement-controlled arc-length scheme, the applied load/displacement of the original has been moved from the centreline to a node near the left hand support, and tilted from the vertical direction by 31.5° (as shown in Fig. 16). The positioning and inclination of this load is rather arbitrary, but is done so that the non-symmetry of the loading results in differing equilibrium paths for the conventional load-controlled arc-length method and the displacement-controlled arc-length method proposed in this paper. The method parameters are the same as in Table 1. A *cylindrical* scheme has been used in the *non-consistent* way. As Fig. 16a shows, the chosen stress-strain relationship is defined by a *Hencky* material, whose axial stiffness is equal to $E^{(1)}A = 50$ MN. The magnitude of the initial values selected for the current study are $\bar{u}_0 = 2$ m and $f_0 = 55$ kN, and the angle of inclination of the displacement/load has been kept constant throughout the analysis. For the sake of clarity, the simulation was stopped after 750 time steps.

As with previous examples, the equilibrium paths represented in Fig. 17 are partial because of the complexity of the bi-dimensional structure. As such, both deflection shapes and animations showing the whole behaviour of the arch are available; the former are shown in Fig. 18, whereas the latter are part of the supplementary material, which is referenced in the acknowledgment section. Fig. 17a shows that the vertical displacement-force curve is entirely different when displacement-controlled or force-controlled analyses are carried out. In the former case, the equilibrium path starts with a peak in force, followed by a

softening, until the local maximum value in displacement is reached at A. The force then decreases and becomes negative, reaching a local minimum in displacement at point B. The structure regains some of its stiffness, achieving a positive force until the local maximum in displacement C is met. This is then followed by a sharp drop in force, with another change in sign of this quantity, whose minimum is denoted by point D. The hardening from D to E is very close to the previous softening from C to D. The same idea applies from E to F, being this very similar to B to C. A steep ascent in force follows point F, with a maximum local value in displacement at G. Continuing the analysis, the maximum value in force can be found after G. From this point, the structure significantly loses stiffness, reaching negative values of displacement and force at H. Another hardening takes place after H until the study is interrupted at the 750th step. The force-controlled analysis represented in Fig. 17a is very different. From its starting point, positive values in force and displacements are achieved, and the curve tends to become flat until a peak in force is met at A'. A softening follows, initially in a gradual way, and later in more significant fashion, reaching a local maximum value in displacement (denoted by B'). The softening continues, decreasing both the displacement and the force, with a local minimum of the latter in C'. From this point, the structure regains stiffness, and a local minimum in displacement D' is accompanied by the maximum value in force, indicated by E'. After this peak, both force and displacement decrease again, and the local minimum of the latter F' is the starting point of a softening curve rather similar to its hardening counterparts (i.e. from C' to D'), which culminates in the local minimum G'. From this point, a gentle hardening continues until the analysis stops.

Considering Fig. 17b, which shows the horizontal force-displacement response of the structure at the loaded/displaced node, the displacement-controlled analysis is quite similar in shape to that presented in Fig. 17a, the main difference being that parts B – C and E – F have now a negative slope. However, if the force-controlled case is considered, it can be seen from the zoom-in in Fig. 17b that the result is radically different in terms of the equilibrium path. The force-controlled curve starts with a negative value of displacement. This tendency continues even after the local maximum in force in A'. However, shortly after this point, the horizontal displacement reverses, but cannot reach a positive value, since the local maximum in displacement B' is still a negative value. A softening of the structure leads to negative values even in force with the minimum at C'. After this point, an S-shaped hardening occurs, with D' and E' being the maximum displacement and force respectively. An S-shaped softening follows as far as G', and this part of the curve intercepts the former hardening part (from C' to D') once close to zero horizontal displacement.

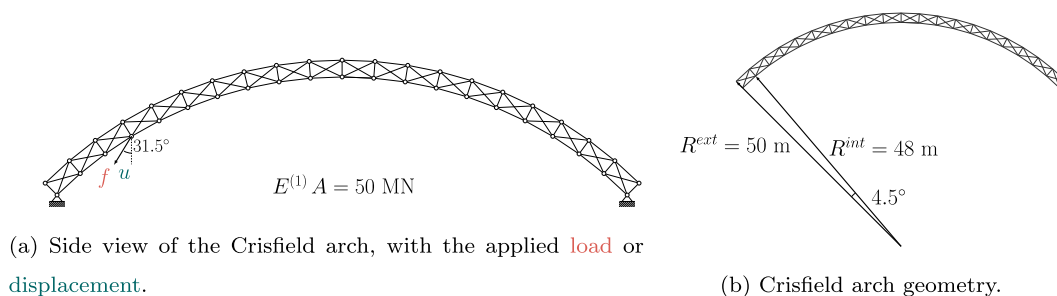
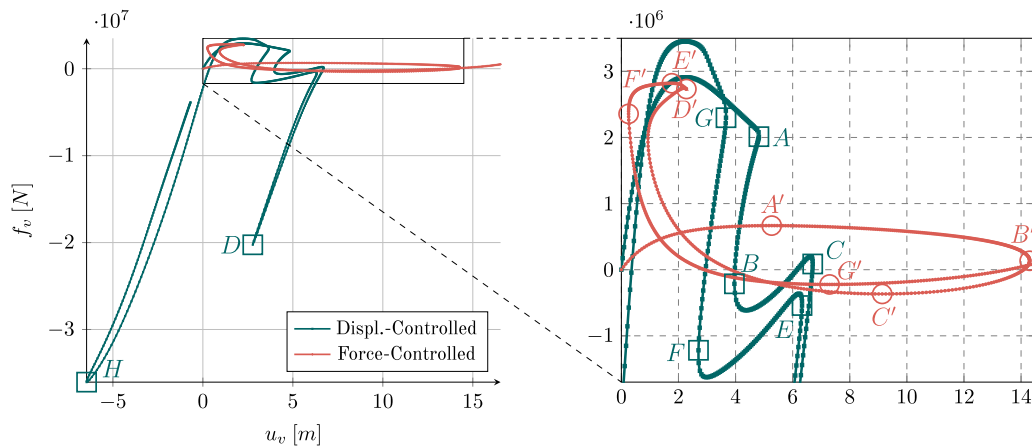
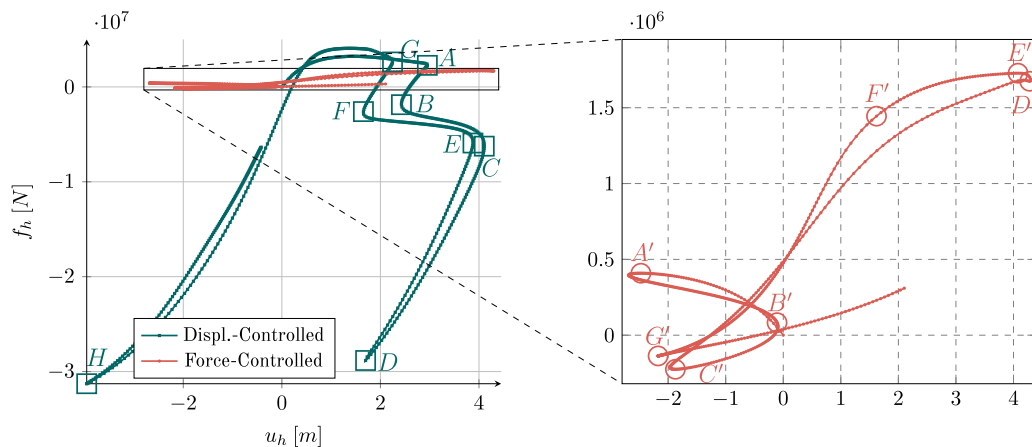


Fig. 16. Crisfield bi-dimensional circular arch.



(a) Equilibrium paths along the vertical direction (left-hand side), and zoom-in view (right-hand side) of rather convoluted parts of the equilibrium curves.



(b) Equilibrium paths along the horizontal direction (left-hand side), and zoom-in view (right-hand side) of a rather convoluted part of the force-controlled equilibrium curve.

Fig. 17. Equilibrium paths of the Crisfield arch.

ment. After G' , the simulation ends with both positive values in force and displacement.

4.5. Cantilever truss structure

In this example, the cantilever truss structure in Fig. 19, is subjected to two compressive and two tensile loads/displacements. This problem has been included to further demonstrate that structures behave differently if displacement-controlled or force-controlled conditions are applied. The analysis parameters are listed in Table 1, and the chosen initial values are $\bar{u}_{z,0} = 0.03\text{m}$ for the displacement-controlled case and $f_{z,0} = 5\text{kN}$ for the force-controlled case. Saint Venant-Kirchhoff material is used.

Before commenting on the behaviour of the structure, it should be noticed that the equilibrium paths for this problem shown in Fig. 20 are inevitably partial since the cantilever truss structure, and consequently its response, are three-dimensional. Hence, to fully understand the results, it is necessary to view the animations of this structure's response which can be found in the supplementary material referenced in the acknowledgement section.

In both cases (i.e. force-controlled and displacement-controlled analyses), monotonically increasing behaviour—from the beginning of the simulation until the peaks A' and A' —is shown for the compressed node in Fig. 20a. Nonetheless, A takes place at a higher value of force and a lower value of displacement than A' . Afterwards, both simulations show a drop in the forces, even though the force-controlled analysis presents a change in sign of this value down to B' . A hardening phenomenon follows in each situation, with B to C being practically linear. In addition, even though the values in forces are quite similar at C and C' , the value of displacement for the latter is significantly higher. A sharp snap-back occurs just after C' , whereas the behaviour following C is smoother. Furthermore, in the displacement-controlled analysis, the response after C presents a tortuous path followed by a local minimum in displacement (denoted by the letter D). In the case of the force-controlled test, the lowest value in force (represented by D') is the starting point of a further hardening, which terminates

⁷ Though it may seem counter-intuitive, in case of displacement-controlled analysis, maxima and minima have to be considered in terms of x-axis values (that is, displacement values), as this is the driven parameter.

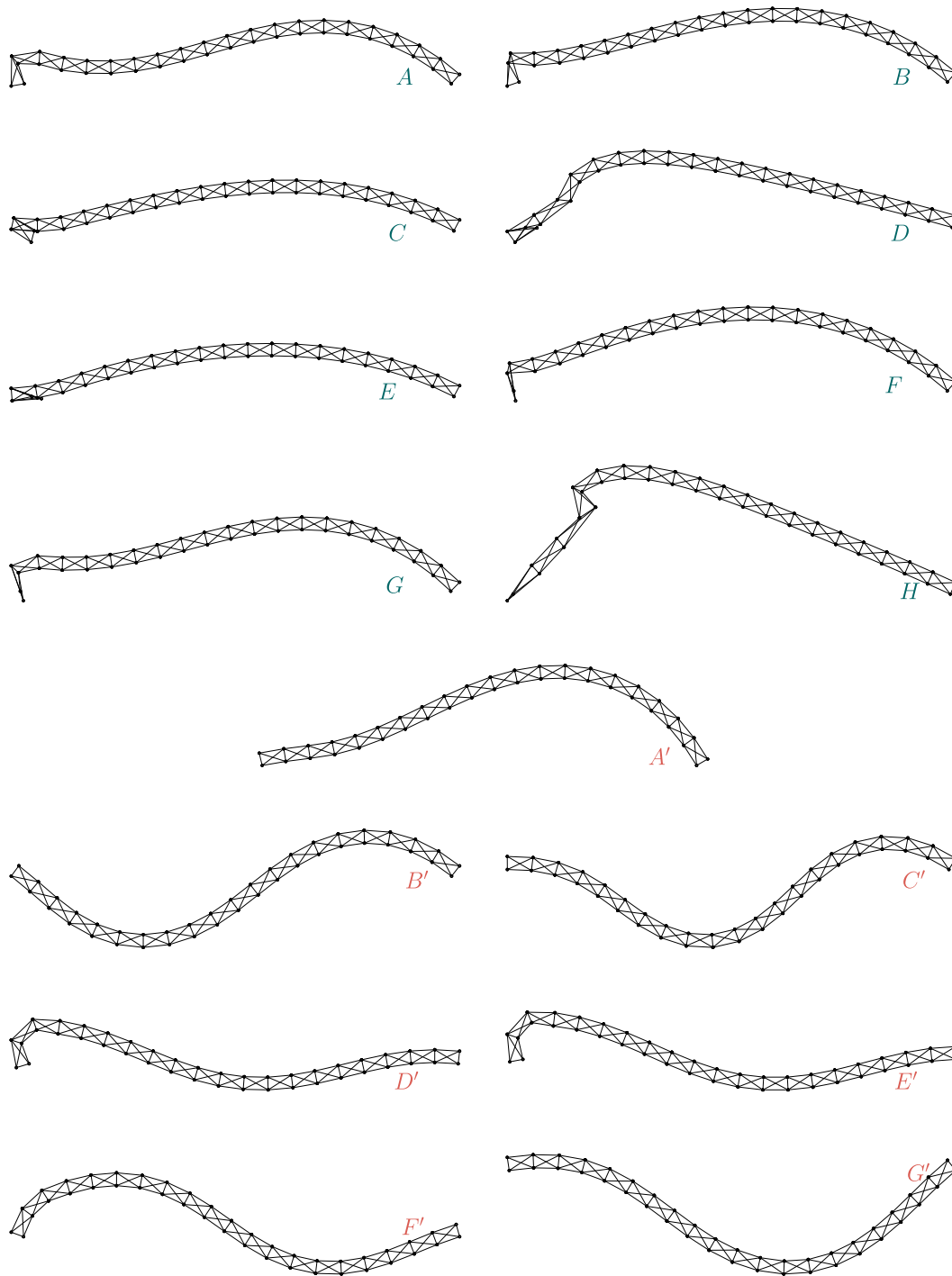


Fig. 18. Deflection shapes of the modified Crisfield arch under displacement control (top rows) and under force control (bottom rows).

to an asymptote following E' . On the other hand, the displacement-controlled analysis shows a minimum in force (denoted by E), followed by an extremely steep part, which corresponds to the whole structure's constrained situation.

If the stretched node is considered (Fig. 20b), the maxima and the minima of the force-controlled test match those of the compressed node (Fig. 20a), is a minimum in force, and this is not the parameter under control in this analysis. Hence, since no *a priori* relationship exists between these forces, they can be a minima/-maxima at one node and not at the other.

the case of displacement-controlled analysis, as shown in Fig. 20b, points A, B, C, and D are again two maxima (A and C) and two minima (B and D). However, it can be seen that point E, in this stretched node, appears to be at quite an arbitrary location. This situation can be explained by the fact that E, in the compressed node (Fig. 20a), is a minimum in force, and this is not the parameter under control in this analysis. Hence, since no *a priori* relationship exists between these forces, they can be a minima/-maxima at one node and not at the other.

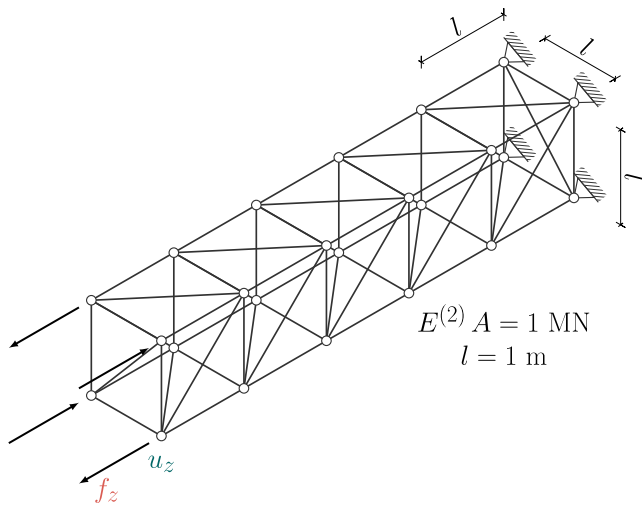
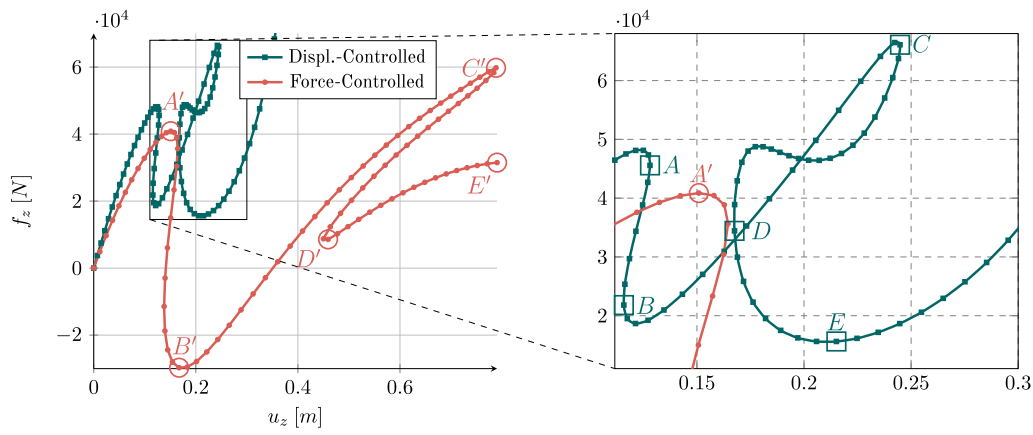


Fig. 19. Cantilever truss geometry and parameters.

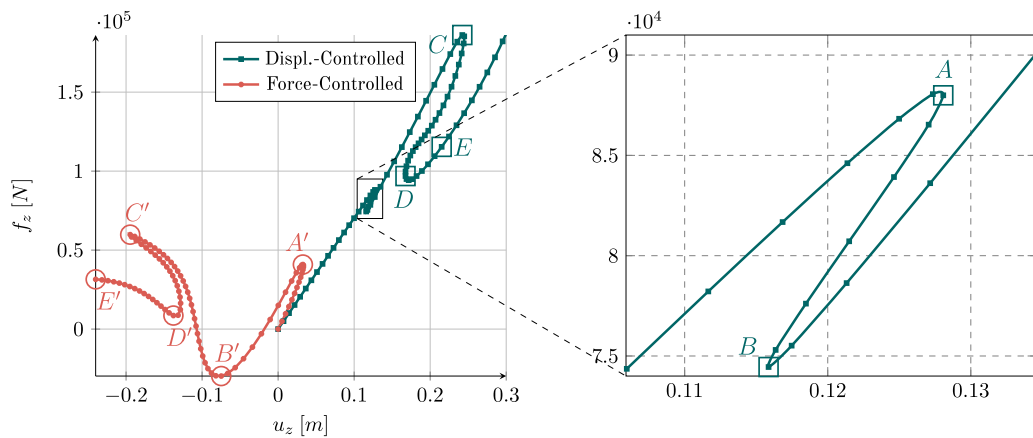
4.6. Continuum cube

The unit continuum cube ($l = 1 \text{ m}$) represented on the left of Fig. 21 is the final example and is included to demonstrate the different responses of a *continuum* body when distinct arc-length schemes (displacement- and force-controlled) are applied. The continuum problem is artificial in nature as it is overconstrained by a poor discretisation, however these issues result in very challenging equilibrium paths in terms of instability. Higher-order shape functions and finer meshes would likely smooth the equilibrium paths shown in Fig. 22, as is to be expected in a continuum discretisation. However, such a non-ideal choice of shape functions and of mesh represents a complex challenge for the studied path-following techniques. Furthermore, it should be highlighted that a monotonically increasing displacement-controlled technique would not be able to follow the equilibrium paths (see Fig. 22) due to the presence of snap-backs.

Three of the cube faces are restrained with roller boundary conditions, one in each direction. A vertical and a horizontal force or displacement has been applied on a free corner, as shown in



(a) Equilibrium paths in the compressed node (left-hand side), and zoom-in view (right-hand side) of a rather convoluted part of the displacement-controlled equilibrium curve.



(b) Equilibrium paths in the stretched node (left-hand side), and zoom-in view (right-hand side) of a rather convoluted part of the displacement-controlled equilibrium curve.

Fig. 20. Equilibrium paths of the cantilever truss-element.

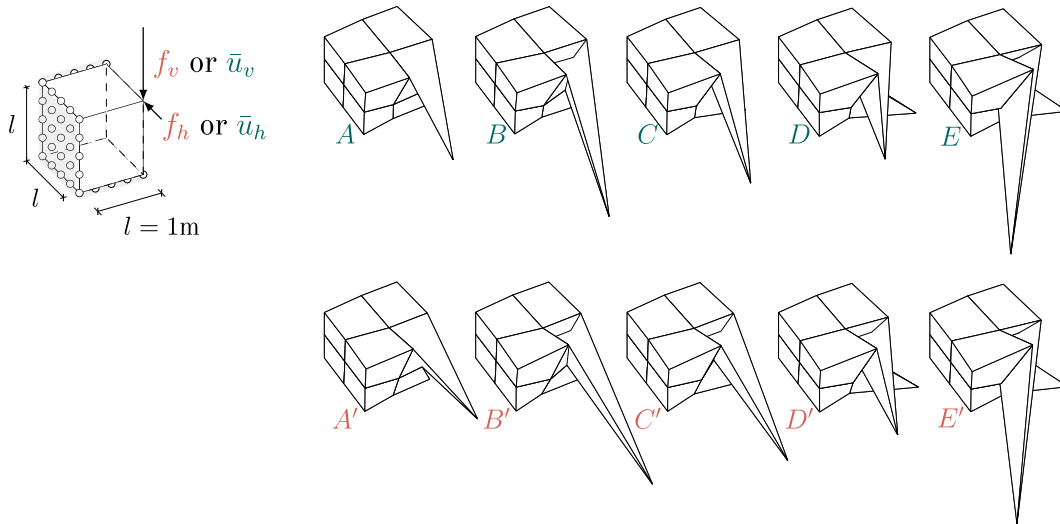


Fig. 21. Original (on the left) and deformed configurations (on the right) due to the displacement-controlled (top row) and to the force-controlled (bottom row) analyses. Letters which define the different layouts are referred to Fig. 22.

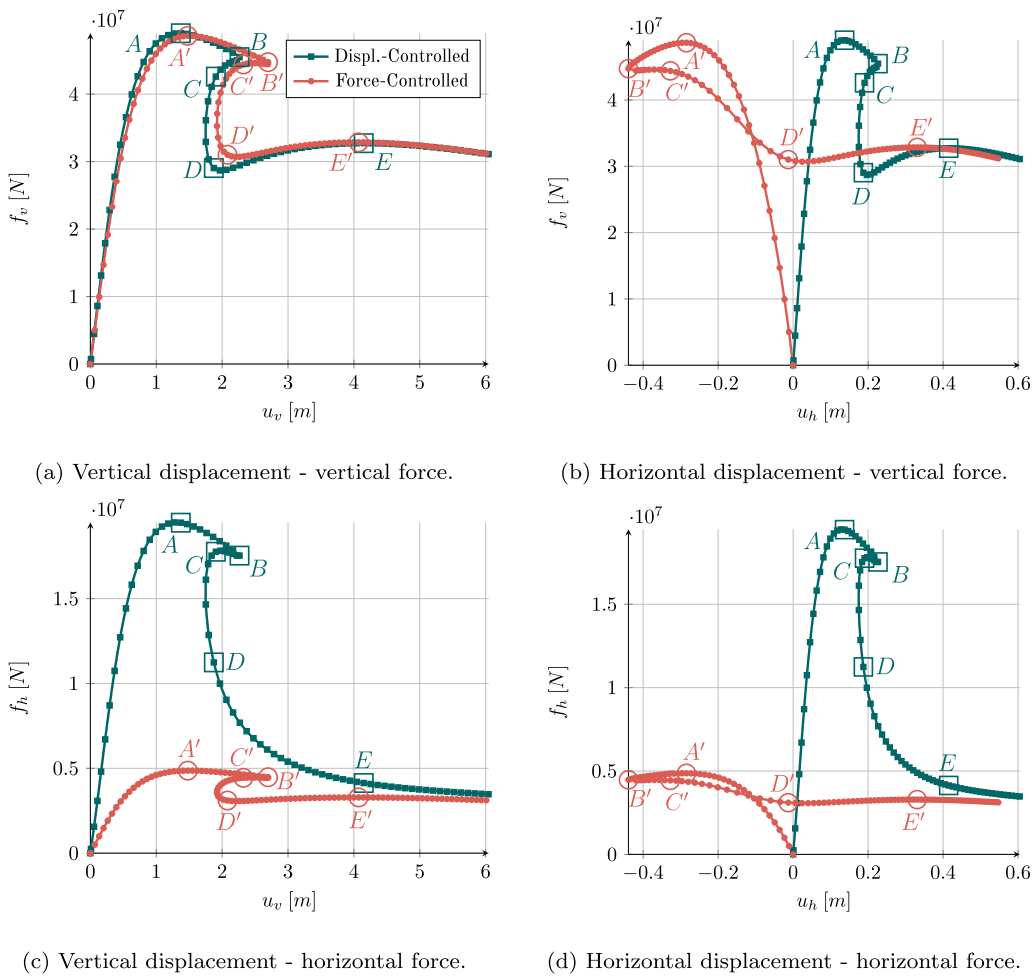


Fig. 22. Continuum cube load-displacement response.

Fig. 21. In particular, the ratio between these quantities is $f_h = \frac{f_v}{10}$ or $u_h = \frac{u_v}{10}$. The cube is made up of Hencky material, characterised by a Young's modulus $E^{(1)} = 10^9$ MPa and by a Poisson's ratio of $\nu = 0.2$. The discretisation of the cube consists of 8 hexahedral elements with tri-linear shape functions and two Gauss points per direction. The studies start with an initial vertical force $f_{v,0} = 5$ MN and initial vertical displacement $\bar{u}_{v,0} = 1$ m, and the *non-consistent* scheme with *cylindrical* constraint has been applied in both cases. Once again, the parameters related to the convergence and to the adopted model are listed in Table 1.

It can be observed from Fig. 22a that the equilibrium paths derived from a displacement-controlled or a force-controlled analysis are quite similar when the response of the cube is considered in the $u_v - f_v$ plane: the behaviour is initially linear, with a peak in responses (A and A'), which are almost coincident, and they both contain a sharp snap-back at B and B' . After these kinks, the force-controlled behaviour predicts a constant force snap-through, C' , whereas the respective snap-through C shows a decrease in the vertical force for the displacement-controlled test. From C to D and from C' to D' , both of the equilibrium paths show a drop in the force response and minimal variation of the vertical displacement. A minimal hardening in the responses occurs from the local minima D and D' to the local maxima E and E' , where other snaps-through occur.

In displacement-controlled analysis, Fig. 22a can be seen as representative of the overall behaviour of the cube, since the response represented in this figure is very similar to those shown in Figs. 22d. The main differences are highlighted in Figs. 22c and d, where point C has a higher value than B with regards to the horizontal force. In the same figures, it can be seen how D and E do not represent local minimum and maximum: in fact, they are points located on a downward path converging to a horizontal asymptote.

On the other hand, the equilibrium paths illustrated in Figs. 22b and 22d are very different from those in Fig. 22a for the force-controlled analysis. First of all, it can be seen that the initial part of these curves predict a negative horizontal displacement.⁸ This behaviour is confirmed by the deformed configurations A' , B' and C' in Fig. 21, where the corner—on which the boundary conditions are applied—is outside the original plane projection of the cube. Secondly, even though the points A' and B' represent again a snap-through and a snap-back respectively, a quasi-linear softening behaviour can be traced between C' and D' , which is entirely different from the constant behaviour in vertical displacement shown in Figs. 22a and b. As expected, Fig. 22b represents a 1 to 10 scaled graph of Fig. 22a since the ratio between the vertical and the horizontal loads is fixed for a force-controlled analysis.

It is worth emphasising that both of the displacement- and load-controlled techniques struggle to converge in the sharp snap-back defined by points B and B' , employing 8 and 9 iterations respectively. These numbers are unusual when the *Newton-Raphson* procedure is adopted, highlighting the challenging nature of this continuum problem.

5. Conclusions

This paper presents for the first time a Dirichlet arc-length controlled equilibrium path following approach that includes several schemes in terms of how these equations are solved. The method allows displacement constraints to be imposed on problems that include snap-back structural behaviour, which is not possible with

conventional displacement-controlled techniques. Critically, in multi-dimensional problems, such as the examples presented here, controlling displacements instead of forces will result in a different structural response. Moreover, displacement-imposed equilibrium paths cannot be tracked without the current method as the presence of snap-backs will cause the conventional monotonically increasing displacement-controlled technique to fail.

It has been shown that the *non-consistent* (NC) scheme with a spherical arc-length constraint is the most robust and efficient for the problems considered in this paper. However, both of the consistent schemes are also robust provided that they are combined with a spherical arc-length constraint. It is not recommended that a cylindrical arc-length constraint is adopted when solving general problems as the method does not place a constraint on the reaction forces (or corresponding internal forces) that can develop during a time step. The consequence of this is, at best, a much lower *utilisation index* (half or less than spherical methods) for the *non-partitioned consistent* (NPC) method and non convergence for the *non-consistent* (NC) and *partitioned consistent* (PC) methods when analysing more complex problems.

As for performance, Eq. (23) indicates that the NPC scheme adds a row and a column to the Jacobian matrix, whereas the PC and the NC schemes add two subroutines, defined by the grey-boxed parts in Algorithms (2) and (3). Hence, the modifications introduced by the new arc-length method can be regarded as negligible in terms of computing time for large number of degree-of-freedom problems.

Overall, the method proposed in this paper adds another arrow to the digital quiver of non-linear path following techniques in structural mechanics and opens the door to these methods being applied to problems where displacement constraints are the most appropriate physical choice for analysing the problem under consideration. Although this paper has focused on the solution of stress analysis problems, specifically for large deformation mechanics with simple truss and continuum elements, the method can be applied to other element types and physical equations where Dirichlet constraints are required.

Furthermore, the current work could be extended to the analysis of thin-walled structures, as these represent a more challenging task for path-following techniques, and important studies and considerations on slight imperfections in real truss structures could also be a valuable avenue of further research.

Declaration of Competing Interest

The authors declare that they have no known competing financial interests or personal relationships that could have appeared to influence the work reported in this paper.

Acknowledgements

This research was supported by the UKRI Engineering and Physical Sciences Research Council (EPSRC) [Grant No. EP/R004900/1]. The authors also acknowledge the support of Ørsted, in particular the contribution to the supervision of the first author by Marc Marchina Puigvert via the *A New Partnership in Offshore Wind* EPSRC-funded Prosperity Partnerships research project. All data created during this research are openly available at collections.durham.ac.uk/ (specific doi to be confirmed if/when the paper is accepted).

Appendix A. Analytical solutions of the two-member truss under displacement control

For the sake of completeness, the analytical solutions for the two-member truss (Fig. 8a) under displacement control (Fig. 8c)

⁸ Forces and displacements are considered as negative when they are in the opposite directions of the ones plotted in Fig. 21.

are reported here. To the authors' best knowledge, this solution is not available in the current literature.

For any given horizontal and vertical displacements, the current length of the two trusses is known, that is

$$l^{(A)} = \sqrt{(l_0 - \bar{u}_v)^2 + \left(\frac{l_0}{2} + \bar{u}_h\right)^2}; \quad (\text{A.1})$$

$$l^{(B)} = \sqrt{(l_0 - \bar{u}_v)^2 + \left(\frac{l_0}{2} - \bar{u}_h\right)^2}. \quad (\text{A.2})$$

As the problem is mono-dimensional, the deformation gradient of the (i) -th ($i = A, B$) truss can be straightforwardly computed as $F^{(i)} = \frac{l^{(i)}}{l_0}$. Under the assumption of incompressibility $J = 1$, the current area of each truss element becomes $A^{(i)} = \frac{l_0 A_0}{l^{(i)}}$, with A_0 being the initial area. Furthermore, the angles between the trusses' current direction and the horizontal axis can be computed as

$$\tan \vartheta^{(A)} = \frac{l_0 - \bar{u}_v}{\frac{l_0}{2} + \bar{u}_h}; \quad (\text{A.3})$$

$$\tan \vartheta^{(B)} = \frac{l_0 - \bar{u}_v}{\frac{l_0}{2} - \bar{u}_h}. \quad (\text{A.4})$$

All the above-mentioned quantities being known, the computation of the forces acting along the axis of the beam $f^{(i)}$ depends on the chosen stress-strain relationship. If the *Hencky* model is considered, the Kirchhoff stress $\tau^{(i)}$ and the logarithmic strain $\epsilon^{(i)}$ are necessary to compute these forces

$$\epsilon^{(i)} = \ln \left(\frac{l^{(i)}}{l_0} \right); \quad (\text{A.5})$$

$$\tau^{(i)} = E^{(1)} \epsilon^{(i)}; \quad (\text{A.6})$$

$$f^{(i)} = \tau^{(i)} A^{(i)}. \quad (\text{A.7})$$

If, on the other hand, the *Saint Venant-Kirchhoff* material is considered, the computation of the Green-Lagrange strain tensors $\mathbb{E}^{(i)}$ and of the second Piola-Kirchhoff stress tensors $S^{(i)}$ must be calculated as

$$\mathbb{E}^{(i)} = \frac{1}{2} \left(\left(\frac{l^{(i)}}{l_0} \right)^2 - 1 \right); \quad (\text{A.8})$$

$$S^{(i)} = E^{(2)} \mathbb{E}^{(i)}; \quad (\text{A.9})$$

$$f^{(i)} = S^{(i)} A^{(i)}. \quad (\text{A.10})$$

Regardless of the choice of the materials described by Eqs. (A.5)–(A.7) and (A.8)–(A.10), the Cartesian reaction forces (f_h and f_v) at the apex node are the sum of the projections of the forces acting along the axis of the beams

$$f_h^{rct} = \sum_i f_h^{(i)} = -f^{(A)} \cos \vartheta^{(A)} + f^{(B)} \cos \vartheta^{(B)}; \quad (\text{A.11})$$

$$f_v^{rct} = \sum_i f_v^{(i)} = f^{(A)} \sin \vartheta^{(A)} + f^{(B)} \sin \vartheta^{(B)}. \quad (\text{A.12})$$

The above forces are considered positive as plotted in Fig. 8c.

Appendix B. Supplementary material

Supplementary data associated with this article can be found, in the online version, at <https://doi.org/10.1016/j.compstruc.2021.106674>.

References

- [1] Alfano G, Crisfield M. Solution strategies for the delamination analysis based on a combination of local-control arc-length and line searches. *Int J Numer Meth Eng* 2003;58(7):999–1048.
- [2] Arena G, Groh RMJ, Brinkmeyer A, Theunissen R, Weaver PM, Pirrera A. Adaptive compliant structures for flow regulation. *Proc Roy Soc A: Math Phys Eng Sci* 2017;473(2204):20170334.
- [3] Barbieri E, Ongaro F, Pugno NM. A j-integral-based arc-length solver for brittle and ductile crack propagation in finite deformation-finite strain hyperelastic solids with an application to graphene kirigami. *Comput Methods Appl Mech Eng* 2017;315:713–43.
- [4] Bathe K. *Finite element procedures*. Prentice-Hall; 1996.
- [5] Batoz J, Dhett G. Incremental displacement algorithms for nonlinear problems. *Int J Numer Meth Eng* 1979;14(8):1262–7.
- [6] Bellini P, Chulya A. An improved automatic incremental algorithm for the efficient solution of nonlinear finite element equations. *Comput Struct* 1987;26(1–2):99–110.
- [7] Belytschko T, Liu W, Moran B, Elkhoddy K. *Nonlinear finite elements for continua and structures*. John Wiley & sons; 2013.
- [8] Bonet J, Wood R. *Nonlinear continuum mechanics for finite element analysis*. Cambridge University Press; 1997.
- [9] Carol I, López CM, Roa O. Micromechanical analysis of quasi-brittle materials using fracture-based interface elements. *Int J Numer Meth Eng* 2001;52(1–2):193–215.
- [10] Carrera E. A study on arc-length-type methods and their operation failures illustrated by a simple model. *Comput Struct* 1994;50(2):217–29.
- [11] Crisfield M. The automatic non-linear analysis of stiffened plates and shallow shells using finite elements. *Proc Inst Civ Eng* 1980;69(4):891–909.
- [12] Crisfield M. A fast incremental/iterative solution procedure that handles snap-through. *Comput Struct* 1981;13(1):55–62.
- [13] Crisfield M. An arc-length method including line searches and accelerations. *Int J Numer Methods Eng* 1983;19(9):1269–89.
- [14] Crisfield M. *Non-linear Finite Element Analysis of Solids and Structures*. John Wiley & Sons Ltd.; 1991.
- [15] de Borst R, Crisfield MA, Remmers JJC, Verhoosel CV. *Non-Linear Finite Element Analysis of Solids and Structures*. John Wiley & Sons Ltd.; 2012.
- [16] de Souza Neto E, Feng Y. On the determination of the path direction for arc-length methods in the presence of bifurcations and 'snap-backs'. *Comput Methods Appl Mech Eng* 1999;179(1):81–9.
- [17] Diaconu CG, Weaver PM, Mattioni F. Concepts for morphing airfoil sections using bi-stable laminated composite structures. *Thin-Walled Struct* 2008;46(6):689–701.
- [18] Feng Y, Perić D, Owen D. Determination of travel directions in path-following methods. *Math Comput Model* 1995;21(7):43–59.
- [19] Feng Y, Perić D, Owen D. A new criterion for determination of initial loading parameter in arc-length methods. *Comput Struct* 1996;58(3):479–85.
- [20] Findeisen C, Hohe J, Kadic M, Gumbsch P. Characteristics of mechanical metamaterials based on buckling elements. *J Mech Phys Solids* 2017;102:151–64.
- [21] Gao Y, Bower A. A simple technique for avoiding convergence problems in finite element simulations of crack nucleation and growth on cohesive interfaces. *Model Simul Mater Sci Eng* 2004;12(3):453.
- [22] Geers M. Enhanced solution control for physically and geometrically nonlinear problems. part ii—comparative performance analysis. *Int J Numer Meth Eng* 1999;46(2):205–30.
- [23] Geers MGD. Enhanced solution control for physically and geometrically nonlinear problems. part i—the subplane control approach. *Int J Numer Meth Eng* 1999;46(2):177–204.
- [24] Hrinda GA. Geometrically nonlinear static analysis of 3d trusses using the arc-length method. In: *13th International Conference on Computational Methods and Experimental Measurements*; 2007. p. 243–52.
- [25] Kamat M, Watson L, Venkayya V. A quasi-newton versus a homotopy method for nonlinear structural analysis. *Comput Struct* 1983;17(4):579–85.
- [26] Kwok H, Kamat M, Watson L. Location of stable and unstable equilibrium configurations using a model trust region quasi-newton method and tunnelling. *Comput Struct* 1985;21(5):909–16.
- [27] Leon SE, Paulino GH, Pereira A, Menezes IF, Lages EN. A unified library of nonlinear solution schemes. *Appl Mech Rev* 2011;64(4).
- [28] Lu K, Augarde CE, Coombs WM, Hu Z. Weak impositions of dirichlet boundary conditions in solid mechanics: A critique of current approaches and extension to partially prescribed boundaries. *Comput Methods Appl Mech Eng* 2019;348:632–59.
- [29] Malvern L. *Introduction to the Mechanics of a Continuous Medium*. Prentice-Hall series in engineering of the physical sciences. Prentice-Hall; 1969.
- [30] May S, Vignollet J, de Borst R. A new arc-length control method based on the rates of the internal and the dissipated energy. *Eng Comput*; 2016.
- [31] Ning X, Pellegrino S. Imperfection-insensitive axially loaded thin cylindrical shells. *Int J Solids Struct* 2015;62:39–51.
- [32] Pecknold D, Ghaboussi J, Healey T. Snap-through and bifurcation in a simple structure. *J Eng Mech* 1985;111(7):909–22.
- [33] Riks E. The Application of Newton's Method to the Problem of Elastic Stability. *J Appl Mech* 1972;39(4):1060–5.
- [34] Riks E. An incremental approach to the solution of snapping and buckling problems. *Int J Solids Struct* 1979;15(7):529–51.

- [35] Riks E. Some computational aspects of the stability analysis of nonlinear structures. *Comput Methods Appl Mech Eng* 1984;47(3):219–59.
- [36] Ritto-Corrêa M, Camotim D. On the arc-length and other quadratic control methods: Established, less known and new implementation procedures. *Comput Struct* 2008;86(11–12):1353–68.
- [37] Schweizerhof KH, Wriggers P. Consistent linearization for path following methods in nonlinear fe analysis. *Comput Methods Appl Mech Eng* 1986;59(3):261–79.
- [38] Turco E, Giorgio I, Misra A, Dell'Isola F. King post truss as a motif for internal structure of (meta) material with controlled elastic properties. *Roy Soc Open Sci* 2017;4(10):171153.
- [39] Verhoosel CV, Remmers JJC, Gutiérrez MA. A dissipation-based arc-length method for robust simulation of brittle and ductile failure. *Int J Numer Meth Eng* 2009;77(9):1290–321.
- [40] Wempner G. Discrete approximations related to nonlinear theories of solids. *Int J Solids Struct* 1971;7(11):1581–99.
- [41] White S, Weaver P. Towards imperfection insensitive buckling response of shell structures-shells with plate-like post-buckled responses. *Aeronaut J* 2016;120(1224):233.
- [42] Yang Y, Shieh M. Solution method for nonlinear problems with multiple critical points. *AIAA J* 1990;28(12):2110–6.